Journal of the Mechanics and Physics of Solids 103 (2017) 199–220

Contents lists available at ScienceDirect

Journal of the Mechanics and Physics of Solids

journal homepage: www.elsevier.com/locate/jmps

Microstructural heterogeneity in rate-dependent plasticity of multiphase titanium alloys

Zhen Zhang*, Fionn P.E. Dunne

Department of Materials, Royal School of Mines, Imperial College London, Prince Consort Road, London, SW7 2AZ, United Kingdom

ARTICLE INFO

Article history:
Received 30 September 2016
Revised 11 March 2017
Accepted 21 March 2017
Available online 23 March 2017

Keywords:
Rate dependence
Creep
Thermally activated dislocation
Intrinsic anisotropy
Orientation dependence
Crystallographic texture
Morphology
Cold dwell fatigue

ABSTRACT

Polycrystalline rate-dependent plasticity is found to originate from heterogeneous slip system/phase rate response. Micro-mechanism under low stress and low temperature ($T < 0.3Tm$) has been shown to be different from conventional rate sensitivity expectations. Hence the constitutive framework developed is dependent on the crystallographic orientation, properly capturing micro-scale anisotropic rate behaviour.

The intrinsic rate anisotropy of the HCP α prism and basal and BCC β phase slip systems in Ti-6242, recently determined from micro-pillar and crystal plasticity modelling, have been utilised to investigate the structural strain rate sensitivities of colonies, polycrystals, bimodal and basket weave microstructures.

The rate sensitivity of colony structures is dominated by the HCP α phase behaviour, at least for alloys containing up to ~20% volume fraction β phase, and is largely independent of β-lath orientation. The apparent anisotropy of a_1, a_2 and a_3 basal resolved shear stresses in Ti-6242 colonies is shown to originate from the local crystal stress states established as opposed to the $\alpha-\beta$ interfaces.

Texture and $\alpha-\beta$ morphology are shown to affect rate dependence and to corroborate that the basal rate sensitivity is stronger than that for prism slip in Ti-6242. Morphological effects are shown to affect rate dependence but not strongly, but the number of HCP α phase variants in basketweave structures is found to have a significant effect with higher numbers of variants leading to lower strain rate sensitivities. This is potentially important in designing alloys to resist cold dwell fatigue.

1. Introduction

The rate-dependent behaviour of a range of hexagonal close packed (HCP) metals at low homologous temperature ($T < 0.3T_m$) leads to significant creep, stress relaxation and the redistribution of stress, often over short time periods. In the context of near-α Ti alloys, it is of particular significance because of its role in the nucleation of dwell fatigue facets which are found to develop on basal planes oriented within about 10 to 15° normal to loading (Sinha et al., 2006). Even at low temperature (e.g., 20 °C), titanium alloys show strong strain rate-dependent material strength and deformation behaviour (Conrad, 1981) and the resulting rate dependence/creep behaviours are physically and industrially important since

* Corresponding author.
E-mail address: zhen.zhang@imperial.ac.uk (Z. Zhang).

http://dx.doi.org/10.1016/j.jmps.2017.03.012

virtually all titanium components operate across the rate-sensitive temperature range (Adenstedt, 1949; Evans, 1987; Neeraj et al., 2000). Plastic strain developed by rate-dependent viscous ratcheting leads to slip accumulation and under conditions of stress dwell, leads to stress redistribution (or load shedding) in appropriately orientated grain pairs, shortening component life (the dwell debit) substantially (Bache, 2003). Compared to single phase metals, those of multi-phase tend to show higher strengths and a change to the strain rate dependence argued to be related to texture and microstructural morphology (Donachie, 2000; Welsch et al., 1993). Rate-dependent behaviour has been reported for single crystals, polycrystals and multiphase titanium alloys in the literature (Conrad, 1981; Welsch et al., 1993), and is therefore important for the industrially-useful near-α (e.g., Ti-6242) and α-β (e.g., Ti-6246). The former alloy much used in the aero-engine industry, for example, is known to show significant cold dwell fatigue debit.

Crystal orientation-dependent strain rate sensitivity, work hardening rate, and creep behaviour have been reported extensively in single crystalline materials. Inui et al. (1997) found that the critical resolved shear stress for <101> slip depended on the crystal orientation in single crystal TiAl, and they reported the strain rate sensitivity being crystal orientation dependent. At room temperature, strain rate sensitivity was found to be higher in a [$\bar{1}$52]-oriented crystal than that in the [021] direction. Guiu and Pratt (1966) found that the room temperature proportionality limit of strain to stress and work hardening rate of single crystal molybdenum depended remarkably on the crystal orientation. Similar crystal orientation-dependent work hardening/strain rate hardening has been observed in single crystal tungsten (Rose, 1962), single crystal iron (Spitzig and Keh, 1970), and single crystal Cu (Bonneville and Escaig, 1979). Orientation-dependent steady-state creep rate has been found in single crystals of γ' precipitation-hardened nickel-based superalloy (Leverant et al., 1973). Experiments on CMSX-4 nickel-base single crystal superalloy showed orientation-dependent creep deformation for tensile loading within 20° of the <001> direction (Rae and Reed, 2007). Crystal-orientation dependent strain rate/creep behaviour has been related to directional cross-slip operation (Bonneville and Escaig, 1979) or a process involving the nucleation, propagation and termination of a specific dislocation structure (Rae and Reed, 2007).

For HCP crystals, Weertman (1983) found polycrystalline and single crystal ice in a hard orientation led to creep rates about 500 times lower than that for soft glide. Orientation dependent room temperature yield stress has been found in single crystal ternary Ti3Al-V alloys (Umakoshi et al., 1993) and critical resolved shear stress (CRSS) for the {1010}<1210>-slip showed a violation of Schmid law. Gu et al. (1994) presented orientation-dependent cyclic deformation in single crystal high purity titanium; when orientations were favourable for double and multiple slip, cell structures were found and the cyclic strain hardening rate was high. Due to the orientation-dependence, the measurements of strain rate sensitivity were used to identify twinning and changes in deformation mechanisms in a Mg AZ31 alloy over a wide range of temperatures and grain sizes (Korla and Chokshi, 2010).

In single crystals of pure metals, the orientation effect on rate-dependent deformation was argued to be caused by dislocation kinks and jogs that depended on the orientation (Thornton and Hirsch, 1958). TEM studies have shown wavy dislocation networks in HCP basal slip but planar slip in prismatic slip systems in single crystal Ti-Al alloys (Williams et al., 2002). This was also observed in a Ti-6242 alloy (Jun et al., 2016b; Zhang et al., 2016c) for which the intrinsic strain rate sensitivities for the basal and prismatic slip systems are very different, and that single crystals of Ti-6242 therefore show strongly anisotropic strain rate sensitivity. In addition, the (bcc) β phase within colonies of Ti-6242 has also been shown to be rate sensitive at low (20 °C) temperature (Zhang et al., 2016b).

It is reasonable, therefore, to anticipate that strain rate sensitivity is also dependent on crystallographic texture in polycrystals, such that it may vary when texture evolves (Canova et al., 1988). The strain rate sensitivity exponent m (where $m = \frac{d\log\sigma}{d\log\dot{\varepsilon}}$) for textured ultrafine-grained aluminium films (with mean grain size ~275 nm) was found to be 0.017, more than six times lower than that for the non-textured film ($m = 0.103$) (Izadi and Rajagopalan, 2016). As a result, flow stress increased by 14% for (110) textured films when strain rate increased from $\sim 7 \times 10^{-6}\,s^{-1}$ to $5 \times 10^{-3}\,s^{-1}$ whereas this was amplified by more than 90% over a similar strain rate range for non-textured films. The mechanistic link between single crystal strain rate sensitivity to that for textured polycrystals has not yet been thoroughly addressed.

In addition to texture, microstructural morphology in multiphase alloys also leads to strong heterogeneous stress and plastic strain fields and hence local mechanical behaviour, including grain-level stress redistribution from rate-dependent deformation (Evans, 1998). Differing morphological microstructures can be obtained by thermomechanical processing (Weiss and Semiatin, 1998, 1999). For example, aligned α colonies may be formed as a result of slow cool, with the size of the aligned α colonies set by the prior β grain size (Conrad et al., 1961). As shown by Lutjering (1998), varying the cooling rate from the β phase field on lamellar microstructures of Ti-6242 can lead to a colony structure (1 °C/min) or to basket weave structure (8000 °C/min). By control of deformation and recrystallization in the $\alpha+\beta$ phase field, where the recrystallization temperature determines the volume fraction and size of equiaxed primary α phase, it is possible to achieve bimodal/duplex microstructures, showing equiaxed primary α grains surrounded by secondary α laths and β plates.

The morphological structure established through cooling rate, whether globular, colony, basket-weave, Widmanstätten or bimodal equiaxed, substantially affects the creep response and rate-dependent yield strength. Conrad and Wiedersich (1960) established the relationships between cooling rate and creep resistance in Ti-25Al-10Nb-3V-1Mo. Generally, the β solution-treated colony-type (slow cooled) microstructure showed superior creep resistance, and the strain-rate dependence of room temperature tensile strength was dependent on the microstructure. Cho et al. (1988) reported that cooling rates from the solutionizing temperature had a major influence on the subsequent creep rates in Ti-6242. Higher cooling rate can introduce decreasing α-β spacing, which has been argued to lead to improved creep resistance. It can result in finer α lath spacing in Ti-6242, and improved creep properties (Viswanathan et al., 2002). Miller et al. (1987) have studied the

mechanical properties of Widmanstätten microstructures in Ti-6Al-2Nb-1Ta-0.8Mo alloy and concluded that larger colony sizes lead to higher creep strains. A smaller colony size provides a shorter distance to accommodate slip and basket-weave structures exhibit no slip compatibility at all. As a result, the room temperature creep rate in colony structures was found to be higher than that in basket-weave structures.

Cold dwell fatigue occurs in a range of near-α titanium alloys but is known to show a much higher dwell debit in alloy Ti-6242 compared with Ti-6246 (Qiu et al., 2014). The α and β phase properties, including intrinsic slip system rate sensitivities, are potentially mildly different across the alloys because of small differences in local chemistries but in fact, recent XRD analysis shows the differences not to be significant. However, what changes very significantly is morphology; for example, Ti-6242 often comprises a duplex globular α/ α-β lath colony structure whereas alloy Ti-6246 shows a basket-weave structure. The discrete dislocation modelling work of Zheng et al. (2016) provided constructive study to explain the differing dwell debits in the two alloys (resulting from the differing rate sensitivities) but did not explicitly examine the α-β morphologies and their link with the rate sensitivity. The discussion above suggests that the rate sensitivities of the two alloys, both at the microstructural unit level and at the averaged macroscale level, are different, predominantly because of the strong morphological differences.

This paper builds from knowledge of the intrinsic Ti α and β phase anisotropic slip system rate sensitivities in order to address single crystal and α-β colony behaviour. It addresses the response of the differing microstructure-level morphological units (colony to basket-weave) and their role in determining strain rate sensitivity, which is pivotal in local stress redistribution (load shedding) from soft to hard units in dwell fatigue. A systematic study is also presented on the role of β lath morphology within α-β colonies on local stress states and corresponding Schmid factors such that independent experimental observations of non-Schmid effects have been rationalised and explained. The importance of stress relaxation, or load shedding, in the context of cold dwell fatigue is also discussed.

2. Dependence of α crystal strain rate sensitivity on orientation

Recent work utilising micro-pillar testing coupled with crystal plasticity modelling in single crystals of α Ti-6242 alloy shows that intrinsic rate sensitivities of the basal and prism slip systems are quite different (Zhang et al., 2016b,c), and has enabled their quantification along with that of the α and β slip strengths. The β-phase has also been found to be strain rate sensitive and β-phase slip strength (280 MPa) is not notably different to that for either prism or basal α-slip at 20 °C. The findings from micro-pillar tests for α and β phases suggest strong orientation dependence of strain rate sensitive behaviour in titanium alloys; that is, the behaviour is likely to be highly anisotropic and texture dependent.

The crystal plasticity slip rule developed in the previous work is utilised in this paper because of its careful calibration and success against a considerable data-base of micro-pillar testing (Jun et al., 2016b; Zhang et al., 2016b,c); its applicability for low stress levels where both forward and backward dislocation jumps are important (Caillard and Martin, 2003; Gibbs, 1969; Kocks et al., 1975); and because it has been shown to be effective in cold dwell fatigue problems in titanium alloys used in jet engines (Dunne et al., 2007; Zhang et al., 2015). The intrinsic hcp α (prism and basal) and β slip system rate sensitivities were shown to be controlled by an activation energy ΔF, along with a corresponding activation volume ΔV, both associated with thermally activated dislocation escape from pinned obstacles. The resulting slip rate for a given system is given by

$$\dot{\gamma}^i = \rho_m \nu b^2 \exp\left(-\frac{\Delta F}{kT}\right) \sinh\left[\frac{(\tau^i - \tau_c^i)\Delta V}{kT}\right] \tag{1}$$

where i indicates the active slip system. ρ_m is the density of mobile dislocations, ν the frequency of attempts of dislocations to jump obstacle energy barriers, b the Burgers vector magnitude, k Boltzman's constant, T the temperature, τ^i the resolved shear stress for the activated slip system, and τ_c^i is the corresponding critical resolved shear stress (CRSS). The activation volume may be expressed as $\Delta V = \frac{\gamma_0 b^2}{\sqrt{\rho_o}}$ (Zhang et al., 2015), determining the length scale involved in the thermal activation event for dislocation escape, where ρ_o is the overall obstacle density, and γ_0 is the representative shear strain magnitude which influences the transient creep response.

For ease of algebraic manipulation, the slip rate given in Eq. (1) may be simplified to

$$\dot{\gamma}^i = \eta \sinh\left[\chi(\tau^i - \tau_c^i)\right] \tag{2}$$

where $\eta = \rho_m \nu b^2 \exp(-\frac{\Delta F}{kT})$ and $\chi = \frac{\gamma_0 b^2}{kT\sqrt{\rho_o}} = \frac{\Delta V}{kT}$ both of which are scalar quantities independent of crystal orientation.

The resolved shear stress τ^i for a specific slip system i, in Eq. (2), is determined by the local stress state and the corresponding crystal orientation such that for *uniaxial* loading the resolved shear is

$$\tau^i = \sigma M^i = \sigma(\boldsymbol{L}\cdot\boldsymbol{n}^i)(\boldsymbol{L}\cdot\boldsymbol{s}^i) \tag{3}$$

where the quantity $\boldsymbol{L}$ is the loading direction vector and σ the magnitude of the applied uniaxial stress. M^i is the Schmid factor for the crystal orientation with slip direction $\boldsymbol{s}^i$ and plane normal $\boldsymbol{n}^i$.

Following Evans and Rawlings (1969) and Hirth and Nix (1969), the macroscopic strain rate for an activated slip system is given as

$$\dot{\varepsilon}^i = \rho_m \nu b M^i = \dot{\gamma}^i M^i \tag{4}$$

where v is the average dislocation glide velocity, and b the magnitude of Burgers vector. Elastic strains are considered negligible compared to the plastic strains in what follows. The plastic shear strain rate $\dot{\gamma}^i$ in Eq. (2) can then be written as a direct strain rate $\dot{\varepsilon}^i$ by

$$\dot{\varepsilon}^i = M^i \eta \sinh\left[\chi M^i (\sigma^i - \sigma_c^i)\right] \tag{5}$$

where $\sigma_c^i = \frac{\tau_c^i}{M^i}$ such that

$$\sigma^i = \frac{\tau_c^i}{M^i} + \frac{1}{\chi M^i} \sinh^{-1}\left[\frac{\dot{\varepsilon}^i}{\eta M^i}\right]. \tag{6}$$

where $\sinh^{-1}$ represents inverse hyperbolic sine function.

Eq. (6) makes clear that the flow stress may be written in terms of a rate-independent term (the CRSS) and a strain-rate sensitive term. The contribution of strain rate hardening for strength has been discussed by Seeger (1954). Classically, shear stress is considered to be composed of athermal and thermal parts (Kocks et al., 1975), where the former is credited to the local or short range dislocation interactions which depend on temperature only through the temperature variation of the elastic constants. The latter thermal part is the effective shear stress that facilitates dislocation glide along the slip plane and in overcoming obstacles.

We introduce the conventional 'structural' strain rate sensitivity index, m, which is determined from Eq. (6) as

$$m = \frac{\partial \ln \sigma}{\partial \ln \dot{\varepsilon}} = \frac{\psi}{\sqrt{1+\psi^2}\left[\sinh^{-1}\psi + \chi \tau_c^i\right]} \tag{7}$$

where $\psi = \frac{\dot{\varepsilon}}{\xi}$ and $\xi = \eta M^i = \rho_m v b^2 \exp(-\frac{\Delta F}{kT}) M^i$ which may now be seen to be directional because of the dependence of ξ on the Schmid factor M which in turn depends upon the uniaxial loading direction with respect to the crystallographic orientation.

For ease of discussion, the superscript 'i' indicating a particular slip system is omitted in the following study. From Eq. (5), we obtain

$$\psi = \frac{\dot{\varepsilon}}{\xi} = \sinh\left[\frac{\tau^* \Delta V}{kT}\right] \tag{8}$$

where the effective shear stress $\tau^* = (\sigma - \sigma_c)M = \tau - \tau_c$.

Therefore, Eq. (7) can then be re-expressed

$$m = \frac{\partial \ln \sigma}{\partial \ln \dot{\varepsilon}} = \frac{\sinh\left[\frac{\tau^* \Delta V}{kT}\right]}{\sqrt{1 + \left(\sinh\left[\frac{\tau^* \Delta V}{kT}\right]\right)^2}} \frac{kT}{\tau \Delta V} \tag{9}$$

where τ is the resolved shear stress based on the local stress state such that $\tau = \sigma M$. Eq. (9) shows that the strain rate sensitivity is dependent on local stress state and activation volume, i.e. $m \propto \frac{1}{\Delta V}$ under high stress state ($\tau^* \Delta V \gg kT$) which will be discussed further in this section.

It can be seen from Eq. (7) that the conventional structural strain rate sensitivity index m is implicitly dependent on temperature T as well as crystal orientation. For given strain rate $\dot{\varepsilon}$ and temperature, the orientation-dependent structural strain rate sensitivity in Eq. (7) is governed by activation energy ΔF, and volume ΔV, and Schmid factor M, and at low temperature, activation energy and activation volume do not vary significantly with temperature. Suri et al. (1999) found that in room temperature creep experiments on near-α titanium alloy (Ti-5%Al-2.5%Sn-0.5%Fe), there was no difference in the creep behaviour for two single crystal α samples with two different orientations but having the same Schmid factor. Interestingly, the strain rate exponent m, defined as $m = \frac{\partial \ln \sigma}{\partial \ln \dot{\varepsilon}}$, has been found to be inversely proportional to the activation volume in cubic materials (Meyers et al., 2006; Wang et al., 2006; Wei, 2007). This is also reflected by Eqs. (7) and (9) where χ is a function of activation volume in Eq. (7).

The simplified approach presented for calculating anisotropic single crystal rate sensitivity in Eq. (7) is assessed quantitatively against full field crystal plasticity finite element analyses of single crystals under uniaxial loading. The slip rule properties (Zhang et al., 2016b,c) are summarised in Table 1. The strain rate strengthening predicted by the simple model (Eq. (6)) is compared directly with the full-field finite element analyses and the results are shown in Fig. 1. For the crystal plasticity modelling, only a representative number of analyses is included (because of computational time) for a 20 μm single crystal cube under uniaxial compression, for both basal and prism slip orientations, as indicated in Fig. 2. The single crystal cube is meshed by 2197 ABAQUS C3D20R UEL elements, and the crystal orientations are taken to be the same as those for the pillars generating basal slip (A2) and prismatic slip (A3) detailed in Zhang et al. (2016c). The crystal plasticity model used throughout this study is that already discussed and is temperature- and rate-dependent, and includes lattice rotation updates. More details can be found in Dunne et al. (2007), Zhang et al. (2015, 2016b). Displacement controlled loading is adopted to generate uniaxial compression up to 2% strain. The boundary conditions considered are indicated in Fig. 1(a) to represent unconstrained uniaxial conditions, since the simplified approach at a material point level cannot represent other structural boundary conditions. As demonstrated in Fig. 1(b), the simplified approach contained in Eq. (6) reproduces the

Table 1
Slip rule properties for Ti-6242 single crystal at 20 °C.

Metals		Ti-6242		
Parameters		α-Basal	α-Prismatic	β
ρ_m	μm^{-2}	5.0		5.0
ρ_o	μm^{-2}	0.01		0.01
ν	Hz	1.0e + 11		1.0e + 11
b	μm	2.95e-4		2.86e-4
k	JK^{-1}	1.381e-23		1.381e-23
$\tau_{c0\ (b,p)}$	MPa	270	240	280
ΔF	eV	0.4247	0.5621	0.3304
ΔV	b^3	1.22	11.97	0.0021

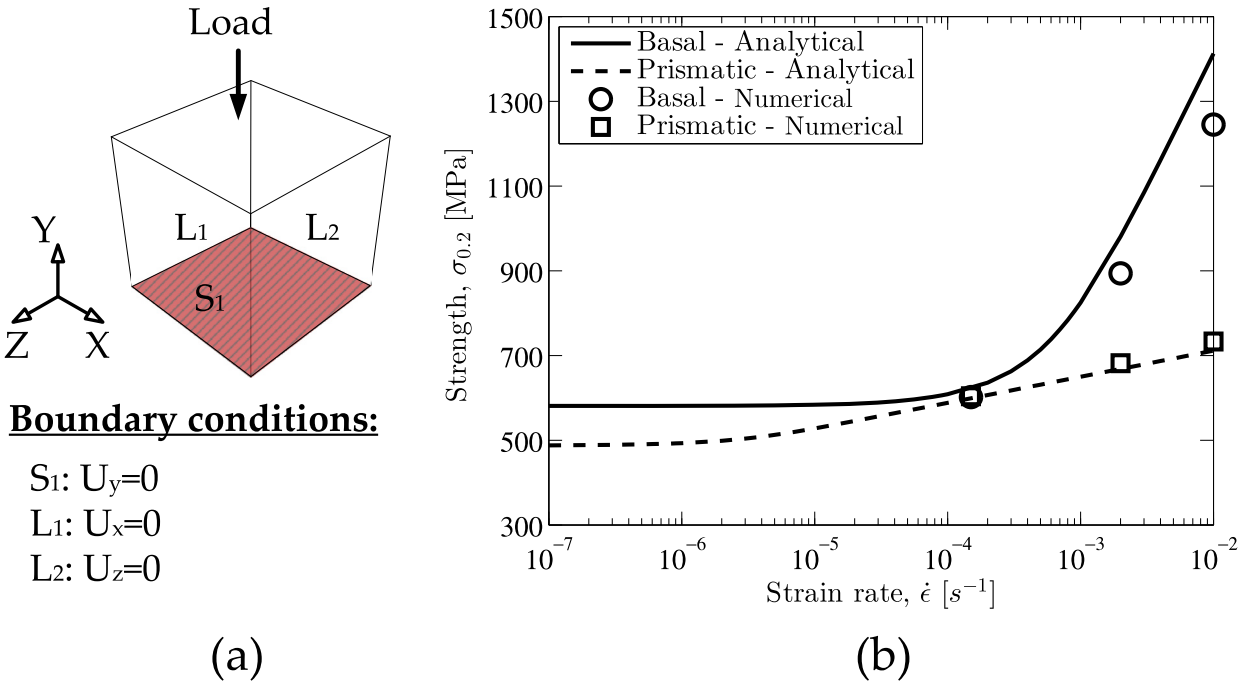

Fig. 1. Comparison of anisotropic rate sensitivities predicted by the full finite element crystal plasticity model (symbols), schematically shown in (a), and those from the simple model approach of Eq. (6) for uniaxial single crystal compression to 2% strain.

observed rate sensitivity trends for both basal and prismatic slip well. Interestingly, both basal and prismatic slip are found to be almost rate independent when the loading strain rate is less than $10^{-5}\,s^{-1}$. At the higher rates, the rate sensitivity associated with basal slip is stronger than that for prism as anticipated from the intrinsic slip system rate sensitivities. Independent recent work by Amouzou et al. (2016) also showed experimentally that strongly textured polycrystals preferring basal slip showed higher rate sensitivities than those textures favouring prism slip.

Utilising the slip properties for α Ti-6242, Eq (7) is employed to investigate the dependence of strain rate sensitivity on crystal orientation for a fixed strain rate of $1 \times 10^{-2}\,s^{-1}$ at 20 °C using this simple approach and the results are shown in Fig. 3. The strain rate sensitivity varies very significantly with basal system activation but shows significantly less sensitivity for prismatic slip system activation, for the particular strain rate considered. Room temperature (20 °C) basal slip in titanium alloys has been shown by Williams et al. (2002) to develop wavy dislocation structures in TEM studies while those for prismatic slip were found to be planar. The three basal slip systems share the same <0001> basal plane normal, whereas those for prismatic slip systems, in contrast, are well separated for the three slip directions and normals. The magnitudes of the strain rate sensitivity index, m, particularly for basal slip are considerably larger than would be anticipated from conventional macroscale polycrystal tests. The methodology for determination of strain rate sensitivity based on assessment of stress relaxation (as opposed to strain-rate controlled) micro-pillar tests presented by Jun et al. (2016b) also led to the extraction of similarly large strain rate sensitivities. It is argued that the absence of boundaries and proximity of free surfaces with very limited constraint are important both in the present single crystal modelling study and for the micro-pillar tests of Jun et al. (2016b). The α titanium alloy considered shows limited strain hardening such that once preferred slip activations have been established, the absence of boundaries encouraging dislocation pile-ups inhibits back stress development and nucleation of new dislocations continues to promote further slip. The rate sensitivity results, therefore, from the intrinsic slip system obstacles pinning gliding dislocations. In contrast, were there additional boundaries to be present (e.g. GBs

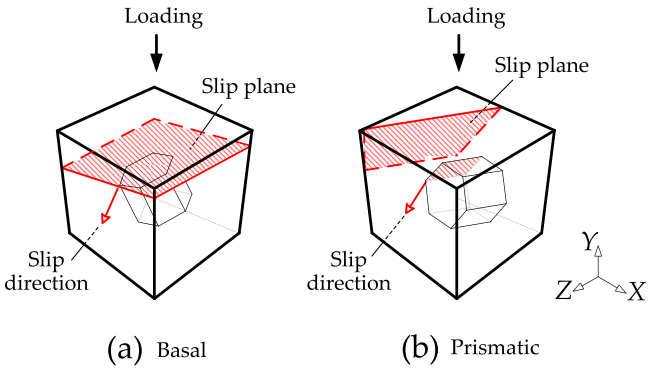

Fig. 2. Schematic diagrams showing crystallographic orientations leading to (a) basal and (b) prismatic slip.

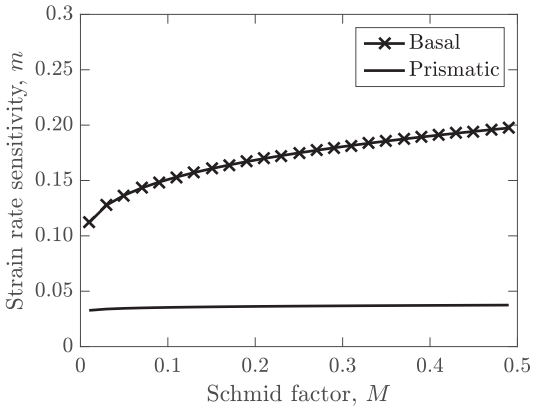

Fig. 3. Dependence of structural strain rate sensitivity on crystal orientations for independent basal and prismatic slip.

in a polycrystal), pile-ups occur, generating back stresses, inhibiting dislocation nucleation from sources, and constraining thermally activated escape and so reducing the macroscale manifestation of rate sensitivity. In the present study, the role of constraint on rate sensitivity is addressed briefly using crystal plasticity in a later section.

2.1. Bounds of crystal slip rule based on backward and forward dislocation movement

The slip rule in Eq. (1) was established considering both forward and backward jumps of thermally activated dislocation escape. This is necessary when kink pairs or jogs are formed in the dislocation loops (Caillard and Martin, 2003; Kocks et al., 1975), which is represented by lattice friction and often associated with ordered alloys. In this study, the backward and forward dislocation movements are determined by the local stress state. There are two important extreme cases which can be considered from Eq. (1), namely when the local effective stress is very high, and only forward dislocation jumps occur (Eyring, 1936; Gibbs, 1969), and when the local stress is low. In the case of high stress, the slip rule simplifies to

$$\dot{\gamma} = \rho_m \nu b^2 \exp\left[-\frac{\Delta F - (\tau - \tau_c)\Delta V}{kT}\right] \tag{10}$$

For the case of low stress (Kocks et al., 1975), it becomes

$$\dot{\gamma} = \rho_m \nu b^2 \frac{(\tau - \tau_c)\Delta V}{kT} \exp\left(-\frac{\Delta F}{kT}\right). \tag{11}$$

These two extreme cases have been independently considered in the context of rate dependent behaviour and stress relaxation studies available in the literature. For both, the stress relaxation which occurs and its associated time constant are investigated (detailed in Appendix A) for a single crystal subjected to uniaxial loading with respect to a specified crystallographic orientation. In addition, the resulting strain rate sensitivities are obtained and compared with those predicted from the full slip rule in Eq. (1). The low stress case (for which both forward and backward dislocation jumps potentially occur) is particularly relevant to the problem of cold dwell fatigue since the in-service stresses are generally low ($<0.9\sigma_y$). The mechanistic basis of basal facet nucleation is argued to depend on local stress relaxation and redistribution (load shedding) through local soft grain (low stress) creep. For this reason, it is therefore important to establish that the slip rule in Eq. (1) appropriately captures the low stress behaviour.

For the case of high stress in Eq. (5), $\frac{\tau^*\Delta V}{kT} \gg 1$ and the governing equation for uniaxial stress relaxation (see Appendix A) becomes

$$\frac{d\sigma}{dt} + \eta EM \exp\left[\chi M(\sigma - \sigma_c)\right] = 0 \tag{12}$$

giving an associated stress relaxation of

$$\sigma(t) = \sigma_c + \frac{1}{\chi M}\left[\ln\frac{1}{EM^2\eta\chi c} - \ln\left(1 + \frac{t}{c}\right)\right] \tag{13}$$

where E is Young's modulus, and c a time-related constant determined from initial conditions, as shown in Appendix A.

Therefore the strain rate sensitivity is given by

$$m = \frac{\partial \ln\sigma}{\partial \ln\dot{\varepsilon}} = \frac{1}{\ln\psi + \chi\tau_c} \tag{14}$$

where $\psi = \frac{\dot{\varepsilon}}{\xi}$ and $\xi = \eta M = \rho_m \nu b^2 \exp(-\frac{\Delta F}{kT})M$.

Given that $\psi = \frac{\dot{\varepsilon}}{\xi} = \exp(\frac{\tau^*\Delta V}{kT})$, Eq. (14) can be rewritten as

$$m = \frac{\partial \ln\sigma}{\partial \ln\dot{\varepsilon}} = \frac{kT}{\tau\Delta V} \tag{15}$$

thereby showing complete consistency with previous analyses of strain rate sensitivity (Asaro and Suresh, 2005; Caillard and Martin, 2003; Evans and Rawlings, 1969; Feltham, 1960; Guiu and Pratt, 1964; Kocks et al., 1975; Wang et al., 2006; Wei, 2007). This is discussed further and later in this section.

For case of low stress, $\frac{\tau^*\Delta V}{kT} \ll 1$ and the stress relaxation is given by

$$\frac{d\sigma}{dt} + \eta EM[\chi M(\sigma - \sigma_c)] = 0 \tag{16}$$

Integrating gives the strain rate sensitivity as

$$m = \frac{\partial \ln\sigma}{\partial \ln\dot{\varepsilon}} = \frac{\psi}{\psi + \chi\tau_c}. \tag{17}$$

For the low stress case, Eq. (8) can be rearranged to show that $\psi = \frac{\dot{\varepsilon}}{\xi} = \frac{\tau^*\Delta V}{kT}$, therefore Eq. (17) may be re-written as

$$m = \frac{\partial \ln\sigma}{\partial \ln\dot{\varepsilon}} = \frac{\tau^*}{\tau} = 1 - \frac{\tau_c}{\tau} \tag{18}$$

It becomes evident that the strain rate sensitivity for low stresses directly depends on the success rate of dislocation escape from obstacles. This barrier is explicitly shown in Eq. (18) as $\frac{\tau^*}{\tau}$, the ratio between local effective stress and the resolved shear stress on the specific slip plane, and demonstrates the rate sensitivity for low stress is fundamentally different from that for high stresses. This is important in the context of cold dwell fatigue, since this occurs at low temperature (the worst case occurs at about 120 °C Zhang et al., 2015) and under low stresses (significantly less than macroscale yield). In this context, the coherent boundaries in titanium alloys make grain boundary or interfacial sliding difficult. The strain rate sensitivity mechanisms in this study are different to those in nanocrystalline (Asaro and Suresh, 2005) and interfacial plasticity induced rate dependence (Zhu et al., 2007), where grain size is small or where grain boundary sliding is important in high temperature and superplasticity prevails.

Fig. 4 shows the three calculations of strain rate sensitivity from the full slip rule (Eq. (9)) and for the two (low and high stress) extremes. The appropriate strain rate regime associated with the low-temperature creep of alloy Ti-6242 is $\sim 10^{-3}$-$10^{-4}\,s^{-1}$ for which $\frac{\tau^*\Delta V}{kT} \approx 0.63$ (Zhang et al., 2016c) so that it becomes clear from Fig. 4 that both forward and backward dislocation jumps are important in dwell fatigue, and both are captured by the slip rule in Eq. (1) (Dunne et al., 2007; Zhang et al., 2015). As the stress increases, the sinh term asymptotes to the exponential form and in this case, the slip rate matches the direct forward dislocation jump rate and backward jumps become negligible.

The strain rate sensitivity may be expressed in terms of direct or shear terms (which are related at the crystal level through the Schmid factor) as

$$m = \frac{\partial \ln\tau}{\partial \ln\dot{\gamma}} = \frac{\partial \ln\sigma}{\partial \ln\dot{\varepsilon}} \tag{19}$$

However, an alternative definition was introduced by Evans and Rawlings (1969) in terms of an effective stress defined as the difference between the applied shear stress and a back stress such that their strain rate sensitivity was found to be given be given by

$$\tilde{m} = \frac{\partial \tau^*}{\partial \ln\dot{\gamma}} = \frac{kT}{V_a} \tag{20}$$

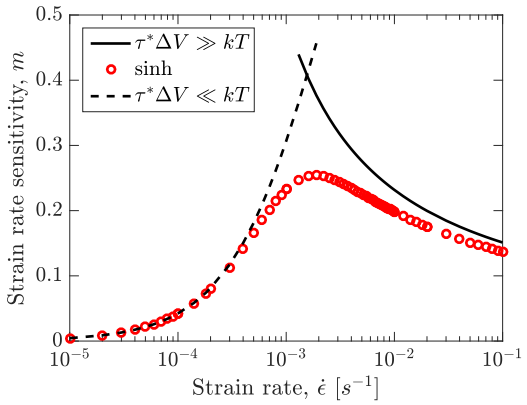

Fig. 4. Bounds for the slip rule based on basal slip properties of Ti-6242 from Zhang et al. (2016c), with a Schmid factor 0.5.

in which V_a is the apparent activation volume. This quantity may be determined from the present crystal slip rule as follows. Firstly

$$m^* = \frac{\partial \ln \tau^*}{\partial \ln \dot{\gamma}} = \frac{\psi}{\sqrt{1+\psi^2}\left[\sinh^{-1}\psi\right]} \tag{21}$$

where the effective shear stress $\tau^* = \tau - \tau_c$. Also, from Eq. (2), $\dot{\gamma} = \eta \sinh[\chi \tau^*]$, so that

$$\psi = \frac{\dot{\gamma}}{\eta} = \sinh(\chi \tau^*). \tag{22}$$

Considering the high stress case such that $\sqrt{1+\psi^2} \approx \psi$, Eq. (21) can be written as

$$m^* = \frac{\partial \ln \tau^*}{\partial \ln \dot{\gamma}} \approx \frac{1}{\sinh^{-1}\psi} \tag{23}$$

Substituting Eq. (22) into Eq. (23) gives

$$m^* = \frac{\partial \ln \tau^*}{\partial \ln \dot{\gamma}} \approx \frac{1}{\chi \tau^*} \tag{24}$$

From above, χ is defined as $\chi = \frac{\Delta V}{kT}$, therefore Eq. (24) can be rearranged as

$$m^* = \frac{\partial \ln \tau^*}{\partial \ln \dot{\gamma}} \approx \frac{kT}{\Delta V \tau^*} \tag{25}$$

For the case of high stress (i.e. $\tau^*\Delta V \gg kT$), the slip rule given by Eq. (10) may be utilised to determine the apparent activation volume of Evans and Rawlings (1969) by

$$V_a = kT \frac{\partial \ln \dot{\gamma}}{\partial \tau} = kT \frac{\partial\left(\ln(\rho_m \nu b^2) - \frac{\Delta F - (\tau - \tau_c)\Delta V}{kT}\right)}{\partial \tau} = \Delta V \tag{26}$$

such that from Eq. (25),

$$m^* = \frac{\partial \ln \tau^*}{\partial \ln \dot{\gamma}} \approx \frac{kT}{\tau^* V_a} \tag{27}$$

Comparing Eqs. (20) and (27), it is apparent that the structural strain rate sensitivity in this work, m^*, determined from the crystal slip rule, is related to the Evans and Rawlings (1969) $\tilde{m}$ by $\tilde{m} = \tau^* m^*$. In summary, the structural strain rate sensitivity presented in Eq. (9) and for high stress in Eq. (15), is consistent with the rate sensitivities of Evans and Rawlings (1969), Caillard and Martin (2003), Kocks et al. (1975), Feltham (1961, 1963), Guiu and Pratt (1964) and Taylor (1992). In addition, the apparent activation volume of Evans and Rawlings (1969) the intrinsic activation volume in the present crystal formulation for the case of high stress states.

3. Morphology and rate effects in α-β titanium alloys

The studies in Section 2 have shown that the strain rate sensitivity depends on crystal orientation. This analysis is extended to investigate the orientation-dependent rate behaviour in α-β colonies, in textured polycrystals, and finally in equiaxed/globular and basket weave morphological variations. The α and β phase stress relaxation behaviour is first examined prior to investigating more complex two-phase microstructures. Simple uniaxial stress relaxation under a strain hold

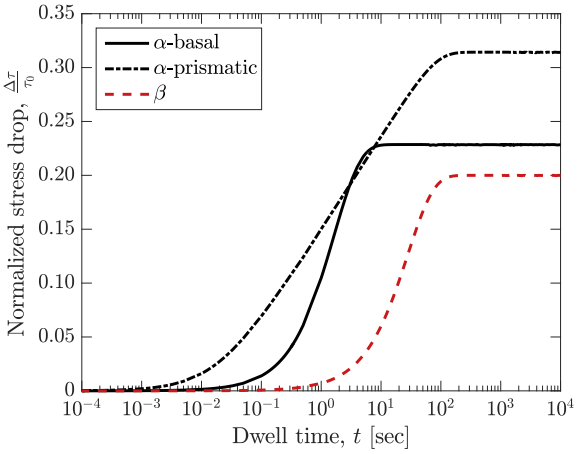

Fig. 5. Stress relaxation for α and β phase slip systems in Ti-6242.

period is considered, utilising the simple model derived in Appendix A, and as discussed earlier for the purpose of obtaining strain rate sensitivity. The properties for the alpha and beta phases are those extracted from micro-pillar tests for both α and β phases (Zhang et al., 2016b,c) and shown in Table 1. Note that pyramidal c+a systems have been reported to have critical resolved shear stresses about 2.5 times larger than those for basal and prism slip (Gong and Wilkinson, 2009), and this is taken to defines the pyramidal slip strengths in this work. Based on our unpublished pillar tests on pyramidal slip systems, their strain rate sensitivity is low compared to prism and basal systems in alpha phase titanium. It is believed pyramidal slip systems play a marginal role in dwell response. Therefore these slip systems are included in the crystal model and treated less rate sensitive than prism slip systems. The shear stress relaxation drop for specified strain hold/dwell time are calculated for individual phases and specified slip systems.

Hold/dwell times from 10^{-4} to 10^{4} s are considered. As shown in Fig. 5, the stresses in all cases are found to saturate after a hold time of 100 s, giving a good indication of the transient time constant. This is close to the two minute macroscale component level dwell fatigue test extensively adopted in titanium alloys (Evans, 1998). The stress decreases are, however, different for each of the α and β systems considered, indicating that the nature of stress redistribution during stress relaxation in α-β colonies is complex and the α-β morphology likely plays an important role in macroscale, averaged polycrystal response (see later).

3.1. Investigation of Ti-6242 colony structures: rate-dependent strength governed by the α phase

Micro-tensile experiments carried out by Savage et al. (2001) on individual α-β colonies of Ti-6242-0.1Si showed that anisotropy existed in "critical resolved shear stresses" of three $a/3 <11\bar{2}0> \{10\bar{1}0\}$ prismatic slip directions and with even more pronounced anisotropy in three $a/3 <11\bar{2}0> \{0001\}$ basal slip systems. The global Schmid factors considered were identically 0.5 for tension and compression tests in the a_1, a_2, and a_3 directions of the α phase in α-β colonies (Savage et al., 2001; Savage et al., 2004). This observation was attributed to the differing ease of α-β slip transmissions caused by Burgers orientation relationships (BORs), and was not thought to be related to the elastic interactions. Anisotropic strength has also been found in Ti-5%Al-2.5%Sn-0.5%Fe (Ti-5-2.5-0.5) by Suri et al. (1999). It was believed to be caused by the relative misalignment of α and β phase slip systems, resulting in the formation of residual dislocations during slip transmission. This may explain the findings of Savage et al. (2004) such that slip transmission from α phase to the β phase in α-β titanium alloys was easiest with respect to the a_1 direction and hardest in the a_2 direction, such that the CRSS was highest for the a_2 direction and lowest for the a_1 direction. However, the volume fraction of the β phase is ~10-15% in α-β Ti-6242 (Williams et al., 2006). Recent studies by Zhang et al. (2016b) show that in colony Ti-6242, the CRSS of β is 280 MPa and very close to α-basal (i.e. 270 MPa) and α-prismatic (i.e. 240 MPa). This suggests that the α-β interface strength may not be the main or only source of the anisotropic α-β colony strengths, so this problem is revisited utilising the Ti-6242 property data determined from micro-pillar compression tests (Zhang et al., 2016b) given in Table 1, together with crystal plasticity modelling. It should be noted that slip transmission across grain boundaries is not explicitly represented within the crystal plasticity framework, but other model formulations such as that of field dislocation mechanics (Acharya et al., 2008).

Unfortunately, the particular α-β colony morphology examined by Savage et al. (2004) is not available so instead, unit cell colony structures of dimensions $10\,\mu m \times 10\,\mu m \times 1\,\mu m$ with a single β lath as illustrated in Fig. 6 are used with a range of β morphological orientations in order to provide bounds which include the experimental configuration, though it is shown later that this is a small effect. A constant volume fraction of 12% β phase is considered to be representative of Ti-6242 alloy (Williams et al., 2006). Hence, the width of the β phase differs with morphological orientation as shown in Fig. 6. Three β lath orientations are considered in order to produce at least one reasonably representative of the Savage et al. (2004) experiment. Periodic boundary conditions are imposed in all models in order to reproduce the confine-

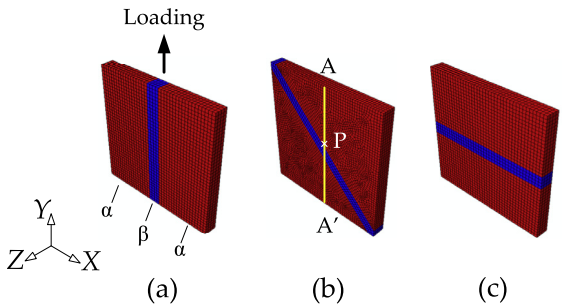

Fig. 6. Unit cell colony structures in $\alpha-\beta$ Ti-6242: (a) vertical β phase; (b) diagonal β phase, with a "P" point 0.3 μm away from the $\alpha-\beta$ interface; (c) horizontal β phase.

ment effect of colonies within polycrystalline material (Abdolvand et al., 2011; Kumar et al., 2006; Mayeur and McDowell, 2007; Pettermann and Suresh, 2000; Van der Sluis et al., 2000).

The experimental crystallographic orientations of α and β phases assessed here are shown in Table b.1 of Appendix B. The α phase orientations can be reproduced by matching the 12 Schmid factors (Savage et al., 2004) of the basal, prismatic and $<c+a>$ slip systems in the model. This is shown in Table b.2 in Appendix B. In addition, the orientation of the β phase can be obtained by enforcing the BOR between α and β phases and simultaneously matching the 24 Schmid factors as far as is possible in the β phase, as listed in Table b.3 in Appendix B. For the following discussion, terminology consistent with that of Savage et al. (2004) is adopted herein to represent the crystal orientations in the α-β colonies. As shown in Table b.2 for the α phase, together with Table b.3 for the β phase associated with the a_1-basal case, the original Schmid factors by Savage et al. (2004) have been well reproduced with the crystal orientations in Table b.1. It remains difficult to determine all crystal orientations unambiguously in all individual α and β phases from matching Schmid factors, as a result of the crystal symmetries in HCP and BCC crystals. This is manifested in the β phase orientation associated with a_2-basal and a_3-basal cases in Table b.3.

The crystal orientations of colonies, i.e. a_1-basal, a_2-basal and a_3-basal, are illustrated in Fig. 7(a)–(c), respectively. Due to the BOR relation, the (0001) basal plane in the α phase (shaded black) is parallel to the $(\bar{1}10)$ plane in the β phase in Fig. 7(a). In addition, the $[11\bar{1}]$ direction out of $<111>$ family in β phase is 10.5° away from the $[\bar{2}110]$ direction in α phase, as indicated in Fig. 7(d). This is illustrated in the pole figure for a_1-basal of Fig. 7(a) as an example; slip planes $\{0001\}_\alpha//<110>_\beta$ are denoted by the agreement of plane normal in red squares in Fig. 7(e) and slip directions $<11\bar{2}0>_\alpha//<111>_\beta$ are identified by the coincidence of green crosses and the a_2 and b_2 directions differ by about 10.5° shown by the green triangular crosses in Fig. 7(f). As shown in Fig. 7(a), for the Y-direction loaded a_1-basal colony, a_1 slip is activated in basal system $[\bar{2}110](0001)$ and its slip normal and slip direction are represented by n_α and s_α, respectively. The activated system in the β phase is $[11\bar{1}](\bar{1}10)$ and the slip plane indicated by red shading with slip normal and slip direction represented by n_β and s_β. The activated slip systems for a_2-basal are shown in Fig. 7(b) and for a_3-basal in Fig. 7(c), respectively. The activated slip systems in these colonies are discussed in due course.

The unit cell colony structures shown in Fig. 6 are loaded in the Y-direction under displacement controlled tension. The tensile loading is applied with a strain rate of $1\times10^{-4}\,s^{-1}$ to a final plastic strain of 4% as in Savage et al. (2004). The experimental methodology to extract resolved shear stresses on the a_1, a_2 and a_3 α slip systems involved measuring the macro-scale 0.2% offset yield strengths and then with knowledge of the global (i.e. assuming a purely uniaxial stress state) Schmid factors, to estimate the local resolved shear stresses (RSS) from $\tau^i = Mi\sigma$. The experimental RSSs for the three basal systems determined in this way (Savage et al., 2004) are shown in Fig. 8. The crystal plasticity colony model allows the a_1, a_2 and a_3 RSSs to be determined in the same way, but also completely and accurately without having to assume a uniaxial stress state applies local to the $\alpha-\beta$ interface. Encouraging agreement with the measurements of Savage et al. (2004) is obtained by replicating the experimental methodology but by using he crystal plasticity modelling approach, as shown in Fig. 8. The RSSs on the a_1 and a_2 basal directions match closely but that corresponding to the a_3 direction less so. This is potentially due to an unknown experimental morphological difference in lath structure adopted by Savage et al. (2004). Possible changes to RSS due to differing colony morphology are investigated from the unit cell model containing a single β lath. As shown in Fig. 8 by the error bar, only negligibly small variations of RSS are caused by the β lath morphological orientation, so this explanation may be discounted. May (2010) repeated the same micro-tensile test using the same Ti-6242 alloy, obtaining a difference in RSS of over 50 MPa which was believed to be caused by unknown morphology effects that were more complicated than the current colony structure with uni-directionally oriented β phase. In Fig. 8, the grey solid lines show the critical resolved shear stresses corresponding to α-basal systems. The dashed grey line indicates the CRSS for the β phase. With the exception of a_1 basal slip, it is found that the RSSs for the active slip systems are really rather different to the CRSSs for both α and β phases. (Recall, however, the methodology – RSSs are determined from knowledge of the macroscale 0.2% proof stress, with the global Schmid factor for each system.) This was explained to be as a result of microstructural-dependent interaction by Ankem and Margolin (1986), leading to positive, negative or zero contribution to 0.2 percent yield strength in α-β titanium.

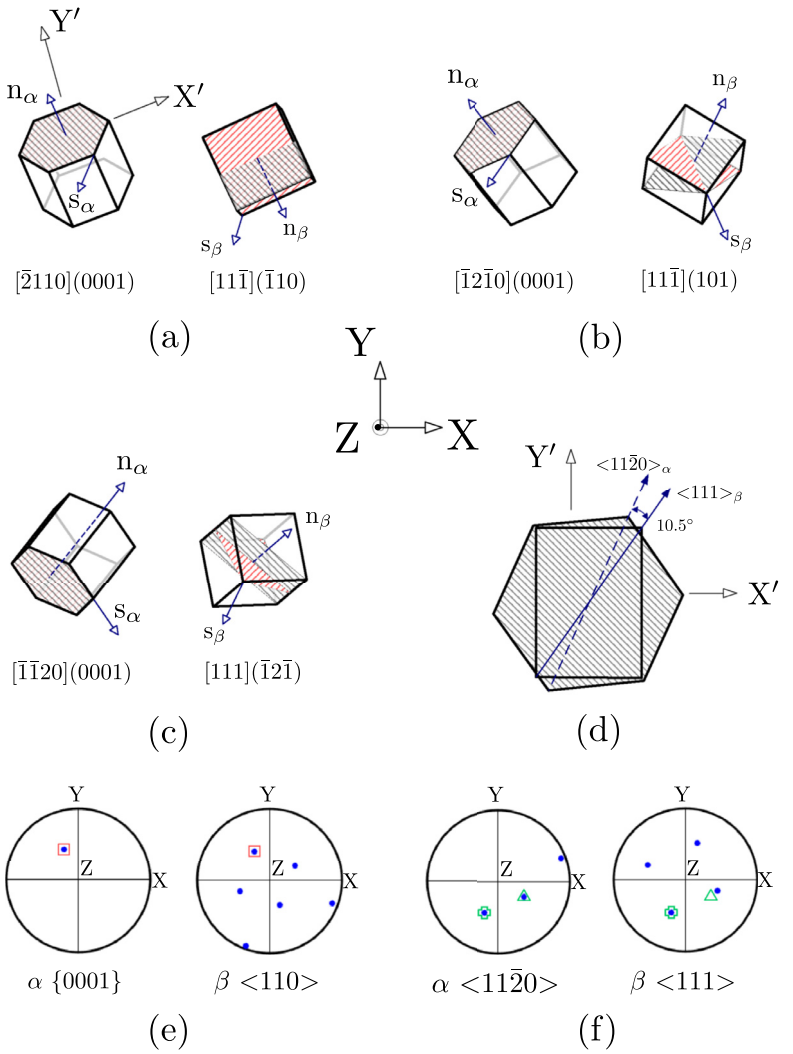

Fig. 7. Crystal orientations in the colony structure unit cell: (a) a_1-basal; (b) a_2-basal; and (c) a_3-basal; (d) the common plane of α and β crystals in BOR relation represented by the black shaded lines and one of the directions of $<111>_\beta$ is 10.5° away from the associated direction in $<11\bar{2}0>_\alpha$. This is demonstrated further in (f), for a_1-basal colony in (a), by the matching of green crosses and 10.5° deviation of green triangular in the pole figure; (e) BOR relation shows planes $\{0001\}_\alpha//<110>_\beta$ and the coincidence of two plane normals are highlighted by the red square. In addition, under loading in the Y-direction of the colonies in Fig. 6, the activated slip systems in the α phase are illustrated in Fig. 7(a)–(c), with slip normal n_α and slip direction s_α, n_β and s_β are the activated slip plane normal and slip direction in β phase, respectively. The activated β slip plane is highlighted by the red shading. (For interpretation of the references to colour in this figure legend, the reader is referred to the web version of this article.)

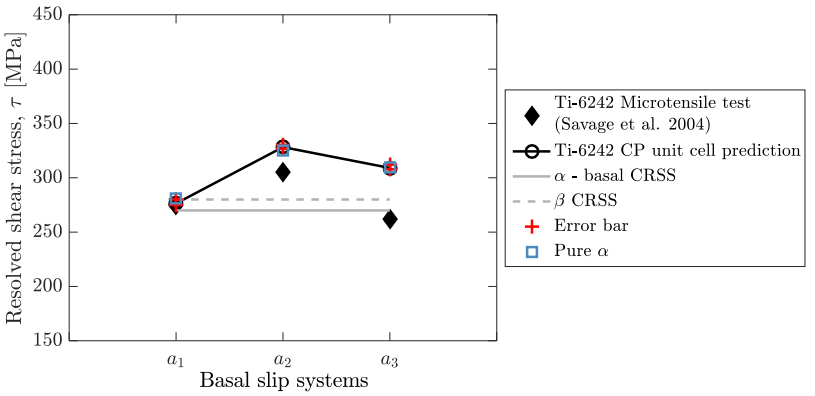

Fig. 8. Dependence of resolved shear stress on the slip directions of activated basal system.

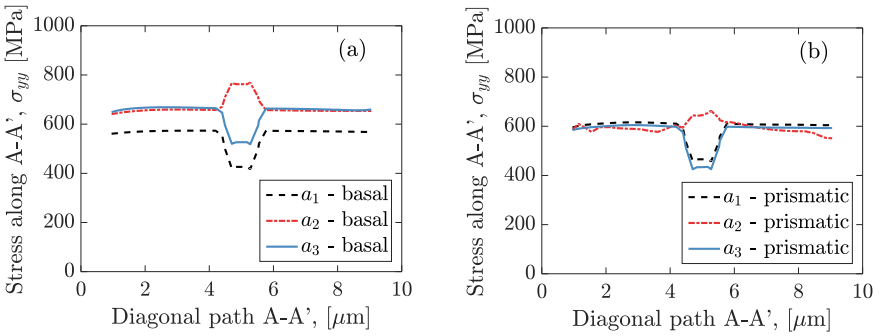

Fig. 9. Interaction stress along the path A-A' in Fig. 6(b) for <a> slip in (a) basal and (b) prismatic systems.

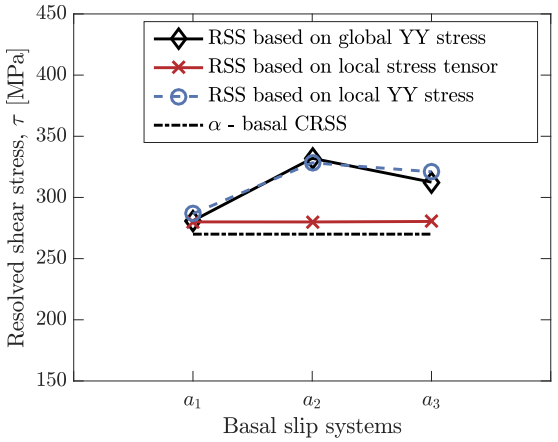

Fig. 10. RSS induced from local stress state and global resultant YY stress. The local location is selected at 0.3 μm away from the interface, i.e. point P in Fig. 6(b).

From the independent experiments by Savage et al. (2004) and May (2010), it has been found that the a_2 basal in the α-β colony has the highest RSS over the a_1 or a_3 basal. In order to investigate this further using the CP model, the α orientation and experimental loading conditions (and periodic boundary conditions) are replicated but in this instance, in the absence of a α-β colony. It is shown in Fig. 8 that the RSSs (determined as above) for the α basals almost completely coincide with the previous model results for the α-β colony unit cell. This indicates that the local strength of the α-β colony structures is governed by the strength of the pure α phase alone. This arises because of the constraint effects developed; in the case of the experiments, by the surrounding colony structures, and in the CP model, by the imposition of periodic boundary conditions to represent the surrounding constraint. The effects of constraint are addressed in more detail below.

3.1.1. Constraint effects on local colony stress states

To examine the role of α-β phase interaction in local stresses discussed in Fig. 8, local YY stresses along path A-A', specified in Fig. 6(b), for a colony with diagonally oriented β phase are investigated. Only this colony configuration is considered since the β phase morphological orientation in the unit cell colony was shown to have negligible influence on the RSS (error bars in Fig. 8). Basal slip in the three directions a_1, a_2 and a_3 is again considered and the crystal orientations of the α and β phase are as before and shown in Fig. 7(a)–(c).

As indicated in Fig. 9, the local stresses activating basal and prism slip across the $\alpha-\beta$ colony vary with alpha crystallographic orientation and hence activated slip system, even though the global Schmid factors for the basal and prism systems are each respectively 0.5. Most notably, the local stress development for the colony with a_2 basal slip is significantly different to a_1 and a_3 slip, resulting from the constraint imposed by the BOR.

A point P is selected as shown in Fig. 6(b), located half of the β phase width away (i.e. 0.3 μm) from the α-β interface. The full local stress tensor $\boldsymbol{\sigma}$ is extracted from the crystal plasticity model when the 0.2% proof stress is applied to the colony structure. The local RSSs can be calculated rigorously from $\boldsymbol{\tau} = (\boldsymbol{\sigma}\mathbf{n}) \cdot \mathbf{s}$, where $\mathbf{n}$ and $\mathbf{s}$ are the updated local plane normal and slip directions respectively. They are shown in Fig. 10 (cross symbols) and are independent of a_1, a_2 and a_3 basal system activated and local stress state; that is, they are close to the CRSS for basal slip. This is, of course, intuitive because the RSS on an activated slip system should transpire to be equal or close to its CRSS (at least for initial slip in the absence of significant hardening). The RSSs are about 280 MPa, and therefore about 10 MPa higher than the corresponding basal CRSS. This results from the strain rate effect – the slip rule in Eq. (1) makes clear that a viscous stress, over and above

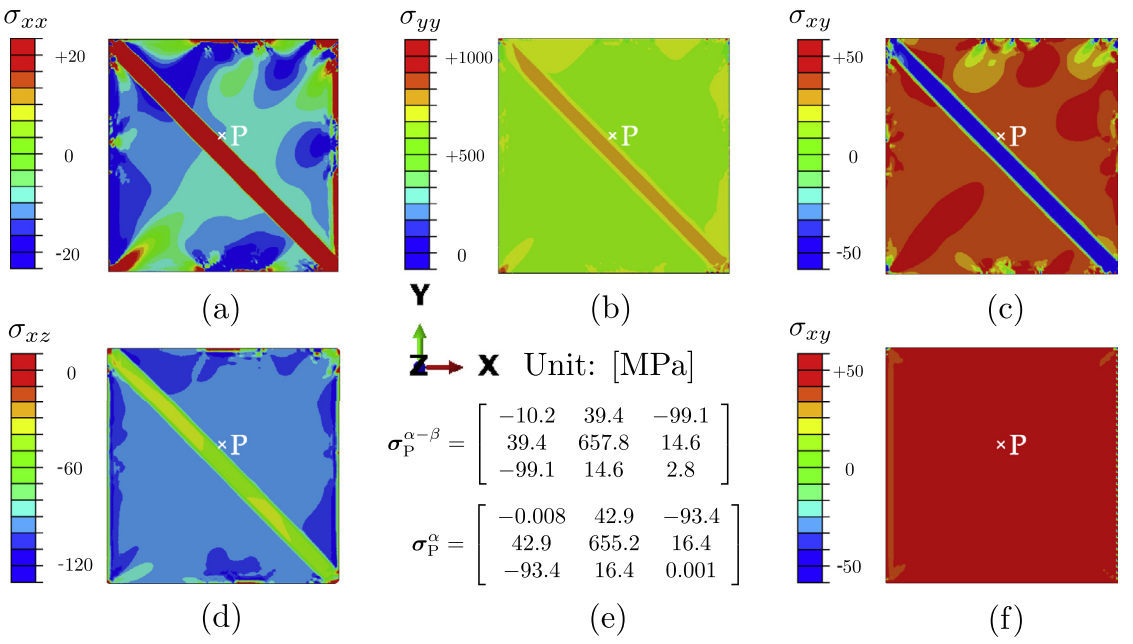

Fig. 11. (a) – (d) Stress tensor components at 0.2% proof stress (673 MPa) loading for α phase a_2-basal colony configuration with diagonally oriented β. (e) local stress tensors at point P close to the $\alpha-\beta$ interface and at the same location but with no β phase included in the model; (f) shows uniform 43 MPa xy- shear stress in pure α phase with the same crystal orientation as that in α of the a_2-basal colony and subject to the same boundary and loading conditions.

the CRSS, develops for rate-sensitive Ti-6242, as also shown in Fig. 1. Fig. 10 also shows the basal RSSs determined assuming a uniaxial stress state (as in the analysis above for Fig. 8), but taking the local YY stress, and the remote global YY stress. Interestingly, they lead to markedly different predicted RSSs to those that actually develop, since the stress state locally is very much not uniaxial. Indeed, it is therefore strongly argued that the apparent anisotropy of basal RSS measured in experiment, and predicted in Fig. 8 is not related to the $\alpha-\beta$ interface (or the β phase) at all, but in fact simply results from the development of non-uniaxial stress states because of the constraint effects (adjacent grains/colonies in the experiment and periodic boundary conditions in the model). It follows that the extraction of RSSs from remote uniaxial applied 0.2% proof stresses by use of global Schmid factors is problematic, as is the interpretation of any local, microstructure-level stress, based on the assumption that the local stress state replicates that of the remote applied loading. Fig. 10 shows that the RSSs determined from the local and global uniaxial YY stresses do differ, but not greatly, as a result of the *local stress state*. The local Schmid factors after deformation are 0.5, 0.4991, and 0.4989 for the α phase a_1, a_2 and a_3 basal systems respectively which are not significantly different to their original values of 0.5 in the undeformed state.

The local stress states giving rise to the differences in apparent and actual RSSs are investigated further in Fig. 11(a)–(d) which show the key local stress components for the a_2-basal colony configuration when it is loaded to achieve the 0.2% proof stress (673 MPa). Due to the constraint imposed by periodicity and because the crystal axes of symmetry do not align with the principal direction of loading, it is found that the stress state developed is not uniaxial. In fact, significant shear stresses are developed of magnitude 50–100 MPa, and it is these stresses which influence the RSSs to generate the differences between the apparent measurements and true values discussed above. Fig. 11(e) shows the stress tensors at Point P for the $\alpha-\beta$ colony model and for the case in which the β phase is not included in the model. This makes very clear that it is the mismatch of principal loading direction with respect to the α crystal orientation, together with periodic constraint which drives the apparent anisotropy in RSSs, which in fact does not derive from the β lath. The corresponding shear stress distribution for the 'colony' model but in the absence of the β phase is shown in Fig. 11(f) showing little change from that in (c) for which the β phase is included.

3.2. *Influence of β phase volume fraction and morphological orientation on structural strain rate sensitivity*

In addition to the phase morphological orientation and crystallographic orientations in the colony structures, the volume fraction of β phase is also important in understanding the colony strain rate sensitivity. Studies are carried out for β phase volume fractions from 5% to 20% in Ti-6242 (Williams et al., 2006). The colony spacing is usually between 3-12 μm with a β-lath thickness of 0.5–2 μm (Savage et al., 2001). A representative colony model, with a size of 50 μm × 50 μm × 2 μm, is shown in Fig. 12(a)-(d) with a colony spacing of 10 μm and β-lath of 1.5 μm. Four β-lath morphological orientations of $\theta = 0°$, 20°, 45° and 90° are considered. The crystal orientations of the α and β phases are chosen from a subset of those used in the previous section; that is the a_2-basal and a_2-prism cases from Table b.1 in Appendix B. Note that the crystal

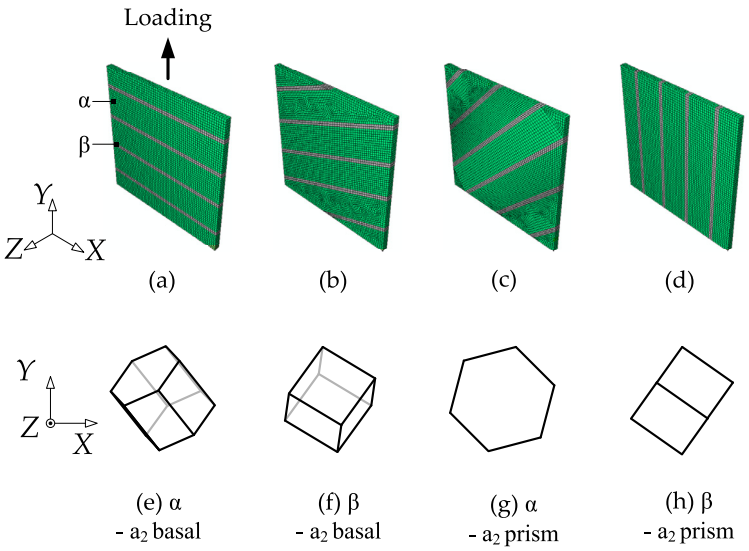

Fig. 12. Unit cell colony structure in Ti-6242 with α phase in green and β phase in grey: (a) horizontal β phase ($\theta = 0°$); (b) inclined β phase ($\theta = 20°$); (c) diagonal β phase ($\theta = 45°$); and (d) vertical β phase ($\theta = 90°$). The BOR relationship is imposed for the two α crystallographic orientations considered - a_2-basal in (e) and (f), and a_2-prism in (g) and (h), for each of the β morphologies in (a) to (d).

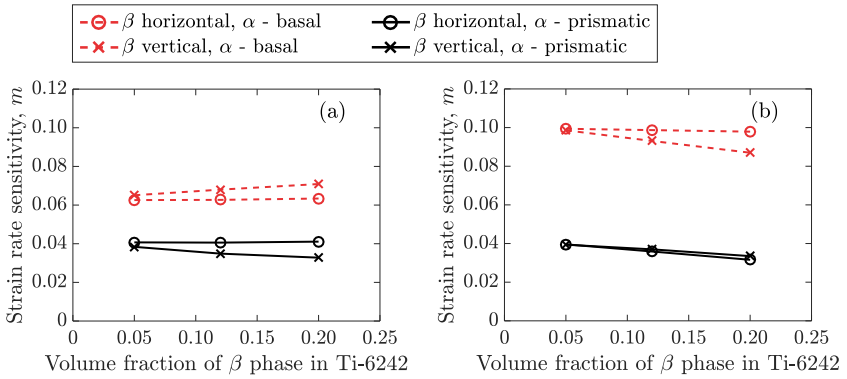

Fig. 13. Dependence of structural strain rate sensitivity on β phase volume fraction (Ti-6242) with horizontal and vertical morphological orientation under Y-direction uniaxial loading for (a) periodic boundary conditions and (b) unconstrained, free boundaries. (For interpretation of the references to colour in the text, the reader is referred to the web version of this article.)

orientation in for the a_2-prism configuration is generated in a similar way to that for a_2-basal such that prism slip occurs in the a_2 direction. The global Schmid factors are 0.5 for the α phase slip systems and the BOR is maintained in all cases for the α-β colony. The $\alpha-\beta$ crystallographic orientation combinations are shown in Fig. 12(e) and (f) for the a_2-basal colony, and in Fig. 12(g) and (h) for the a_2-prism colony. As before, periodic boundary conditions are imposed on the model and constant strain rate loading is applied along the Y-direction with rates of $1 \times 10^{-2}\,s^{-1}$, $1 \times 10^{-3}\,s^{-1}$, $1 \times 10^{-4}\,s^{-1}$ up to a strain of 1%. Strain rate sensitivity is extracted from the constant strain rate sensitivity tests as outlined in Dieter and Bacon (1986), i.e. structural strain rate sensitivity is determined as $m = \frac{d\log\sigma}{d\log\dot{\varepsilon}}$. This measure of strain rate sensitivity is used throughout the rest of this paper, unless otherwise clarified. The selection of the applied strain rates maintains the relevance to dwell fatigue and low temperature creep (Bache, 2003).

3.2.1. β phase volume fraction

The influence of the β phase volume fraction is studied first. Two β-lath morphological orientations are considered initially; specifically, those shown in Fig. 12(a) and (d). With a β-lath thickness is 0.6 μm, the β phase volume fraction then occupies 6% in the α-β colony in Fig. 12(a). By increasing the β-lath thickness, i.e. from 1.5 μm to 2.5 μm, the β phase volume fraction becomes 12% and 20% respectively. Fig. 13 shows the variation of structural strain rate sensitivity with β-lath volume fraction for horizontally and vertically arranged laths. As shown by broken red lines in Fig. 13(a), when basal slip is activated in the α phase, the strain rate sensitivity shows a slight increase with β phase volume fraction. This is seen to be largely independent of morphological orientation of the β phase. When prismatic slip is active in the α phase and the β phase is morphologically horizontally arranged as in Fig. 12(a), strain rate sensitivity decreases slightly with increasing β volume fraction, and this is slightly more significant when the β phase is arranged vertically as in Fig. 12(d). However, the

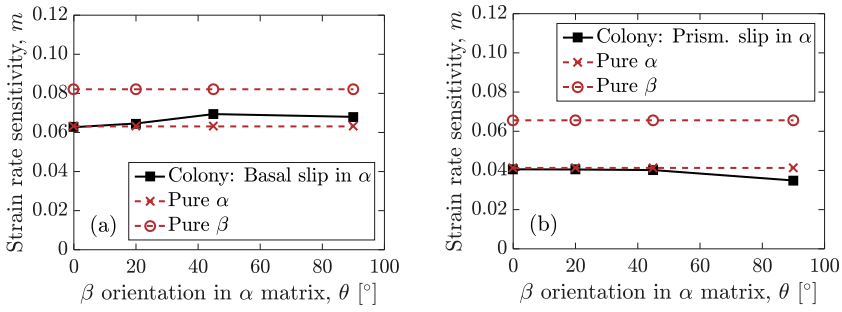

Fig. 14. Dependence of strain rate sensitivity on β phase morphological orientation for basal and prismatic slip activation for a β-lath volume fraction of 12%.

much more significant manifestation is that with basal slip activated, the strain rate sensitivity is much higher than that for prism slip and that this difference far outweighs any effect from β-lath morphology or volume fraction (from 0 to 20%).

The same analyses have been carried out but with right and left colony unit cell model boundaries unconstrained; that is, the periodic boundary conditions are no longer applied, making the analyses closer to representation of single colony micro-pillar tests discussed above. Results are given in Fig. 13(b). Little effect is seen for the case of prism slip for which the structural strain rate sensitivity remains ~0.04. However, the effect for the more rate-sensitive basal slip is quite dramatic with unconstrained uniaxial straining with free boundaries leading to strain rate sensitivities increasing from 0.065 (for periodic boundary conditions) to ~0.1. Dislocation effects, including rate sensitive slip, are likely to be driven by local features of pile-ups. However, the present crystal plasticity model indicates, in an average sense, that rate sensitivities derived from unconstrained, boundary-free, single-crystal testing (e.g. micro-pillar) are anticipated to be substantially higher than those for constrained systems (e.g. polycrystals), and the crystal plasticity model also explains why volume fractions of β phase laths up to 25% do not change this result.

3.2.2. β phase morphological orientation

The volume fraction of β phase is now fixed at a typical 12% for Ti-6242 to focus on the β-lath orientation effect alone. As shown in Fig. 12(a)–(d), a morphological orientation angle of the β-laths is considered varying from 0° to 90°. Fig. 14 shows the strain rate sensitivity results for the cases where (a) a_2-basal slip and (b) a_2-prismatic slip is active in the α phase. The results are shown alongside those obtained for pure α and β phases respectively with the same orientations from the relevant α-β colony. As shown in Fig. 14(a) for basal slip, strain rate sensitivity consistently increases with morphological angle but the changes are very small. This becomes a decreasing trend for the case of prismatic slip in Fig. 14(b) but again, the changes in the magnitude of rate sensitivity are almost negligible for morphological orientation. For the 12% volume fraction of β-laths considered, the much more important conclusion, however, is that it is the α phase which governs the structural strain rate sensitivity for the $\alpha-\beta$ colony. It is shown in Fig. 14 that the rate dependence is not necessarily bounded by that for pure α and β phases. Ankem and Margolin (1986) observed that for α-β Ti-Mn alloys, for 0.2% yield strength, the phase interactions could bring increasing, decreasing, or no influence depending on the microstructure. In this study for the simple colony structures examined, the α phase and its prism and basal intrinsic rate sensitivities are found to dominate structural strain rate sensitivity.

3.3. Polycrystal texture and $\alpha-\beta$ structure effects

The anisotropy in single crystal and slip system intrinsic strain rate sensitivity suggests that structural strain rate sensitivity should be dependent on the texture. In addition, only rather simple morphological effects ($\alpha-\beta$ colonies) have been addressed so far whereas the alloys utilised in service often have much more complex basket weave or Widmanstätten structures (Lütjering and Williams, 2007; Weiss and Semiatin, 1999). Hence in this section of the paper, we address texture effects in α polycrystals, and example complex $\alpha-\beta$ morphologies with respect to strain rate sensitivity.

The strain rate sensitivity is investigated first utilising a model polycrystal with dimensions $200 \times 200 \times 20\,\mu m$ taken from Zhang et al. (2016a). As shown in Fig. 15(a), the polycrystal model contains 120 hexagonal shaped grains and it is discretized by 10,752 ABAQUS C3D20R user elements. The grain size is about 20 µm. The boundary conditions imposed are shown in Fig. 15(a) such that the front surface on the XY plane is unconstrained along the Z axis. To examine texture effects, loading is imposed separately along directions +Y and +X with respect to a given texture. Tensile strain-controlled loading up to 1% is imposed at the three strain rates $1 \times 10^{-2}\,s^{-1}$, $1 \times 10^{-3}\,s^{-1}$ and $1 \times 10^{-4}\,s^{-1}$.

This crystal plasticity texture study incorporates the anisotropic strain rate sensitivity which occurs in the pure α phase due to the intrinsic anisotropy of basal and prismatic slip (properties from Table 1), and the β phase is not explicitly included (but it is later). Five different HCP textures as shown in Fig. 15(b) are examined for the two loading directions, including strong basal textures (1) and (2) (where the textures are the same but simply rotated 90° about the Z-axis), and non-basal texture (3). Textures (4) and (5) are variations on close to random (note the low intensities for these). The strain rate sensitivities determined are shown in Fig. 15(c) and in keeping with the discussion earlier, show that the constraint

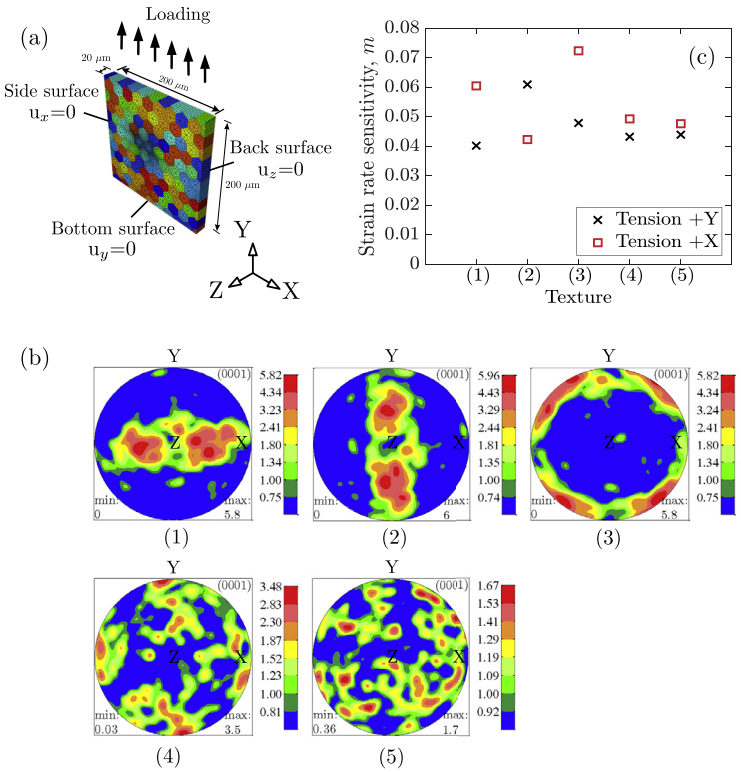

Fig. 15. Dependence of strain rate sensitivity on HCP textures.

imposed by polycrystal deformation (as opposed, for example, to single crystal micro-pillar deformation) inhibits high rate sensitivities such that they are found within the range 0.04 to 0.07. It is also clear that texture can play a significant role in polycrystalline α-Ti strain rate sensitivity. However, the rate-dependent behaviour shows similar behaviour for loading in two orthogonal +Y and +X directions for the random textures (4) and (5). Slightly more separation of strain rate sensitivity was found in texture (4) compared to texture (5). This is due to the stronger texture intensity in the former than the latter, indicating texture (4) is less close to truly random than texture (5). For texture (1), prismatic slip is favoured when tensile loading is applied in the Y direction and basal slip when loading in the X-direction. Therefore the m value is smaller for the former than the latter, as the prismatic system is less sensitive than the basal slip Zhang et al., 2016b,c). This agrees closely with a recent study by Amouzou et al. (2016) who addressed commercially pure polycrystal α titanium which had a texture close to that of texture ((1) considered here. At 1% plastic strain, their experiments showed an increase of 39 MPa in flow stress when the tensile strain rate increased from 5.1×10^{-4} s^{-1} to 8.1×10^{-3} s^{-1} in the TD (+X in this study) direction, larger than the 27 MPa increment of flow stress in the RD (+Y in this study) direction. This indicated experimentally a more rate sensitive response in +X (TD) direction than +Y (RD) direction. More importantly, their results indicated that the basal slip system had to be more rate sensitive than that for prism slip in order to give good agreement between their crystal plasticity model and constant strain rate and work hardening tests. This provides independent corroboration of the intrinsic basal and prism rate sensitivities determined by (Zhang et al., 2016b; Zhang et al., 2016c).

In texture (2), basal slip is preferred when loading in the Y-direction which is a reversal from texture (1). Therefore the m values for textures (1) and (2) switch with loading direction change. In texture (3), crystal orientation favours c+a slip with loading in the Y-direction, but the critical resolved shear stress for these systems is very high (2.5 times that for prism slip) which largely prohibits this system. More basal slip is favoured with loading in the in X-direction.

3.4. Morphology of α and β phases, phase arrangements in Ti-6242 and its role in rate sensitivity

The anisotropic strain rate sensitivities of the α basal and prism slip systems have been shown to affect the structural rate dependence of α polycrystals as a function of texture. In α-β titanium alloys, microstructures can be made to vary very considerably by changing the thermo-mechanical processing route. The latter can generate colony structures, bimodal equiaxed structures, and basket weave structures, as shown in Fig. 16(a), (d) and (g). In this section, the strain rate sensitivities which result from these three representative morphologies in α-β Ti alloys are investigated. The volume fraction of β phase is chosen to be 12% in all the α-β crystal plasticity models considered.

The colony structure in Fig. 16(a) is modelled with dimensions of 50 μm × 50 μm × 2 μm. The geometric representation is shown in Fig. 16(b) together with the crystal plasticity finite element representation in Fig. 16(c). The crystal orientation

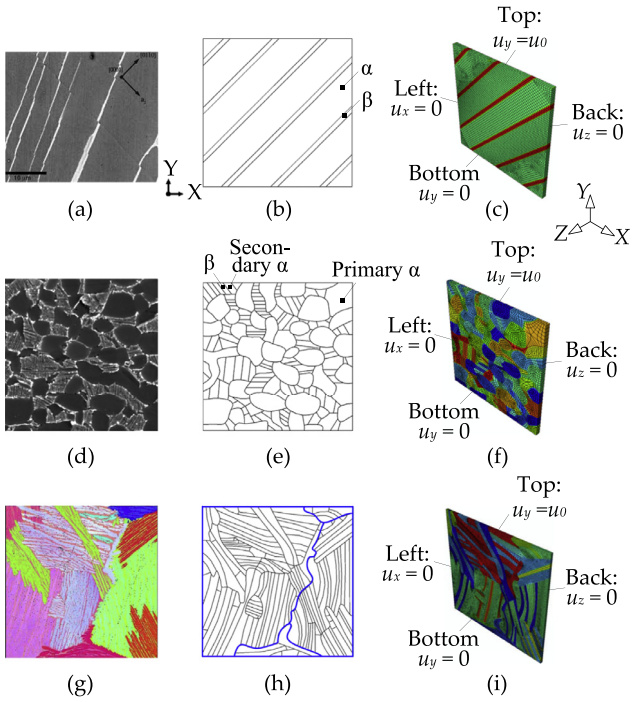

Fig. 16. Models of three microstructures in Ti-6242 showing sequentially the experimental microstructure, the simplified geometrical representation and the crystal plasticity finite element representation for: (a), (b) (c) reference colony structures (Savage et al., 2001); (d), (e), (f) bimodal equiaxed microstructure (by courtesy of Dr Sudha Joseph) and (g), (h), (i) basket weave structures with five α variants in two large transformed β grains (by courtesy of Dr Terry Jun), where (h) shows a geometric sketch of basket weave structure in (g) and transformed β grain boundaries are shown in blue. (For interpretation of the references to colour in this figure legend, the reader is referred to the web version of this article.)

of the α-β colony is taken from the a_2-basal configuration in Table b.1 in Appendix B, where the BOR is implemented between α and β phases. The equiaxed globular microstructure in Fig. 16(d), (e) and (f) contains 47 primary α grains and 54 α-β colony grains. The crystal orientations of primary and secondary α are randomly generated, with the BOR enforced between secondary α and β phase laths. The basket weave structure, as shown in Fig. 16(g)–(i) takes dimensions of 200 μm × 200 μm × 4 μm with four transformed β grains with α variants. The grain boundaries of the transformed β grains are highlighted with blue lines in Fig. 16(h). The α variants are demarcated by differing colours in Fig. 16(g). The dimensions of the basket weave structure selected are larger than the previous colony and equiaxed globular structures and are taken from a representative heat treated Ti-6246 sample. The crystal orientations of the β laths and α variants are taken from EBSD maps scanned from a sample of alloy Ti-6246 (Jun et al., 2016a). The BOR is enforced within the basket weave microstructure. As shown in Fig. 16(g) when compared to Fig. 16(h), the five α variants are shown in turquoise, light blue, green, deep red, and light purple colours in the largest left transformed β grain. Only two α variants are contained in the right transformed β grain. Fig. 17 shows the pole figures corresponding to the left transformed β grain for its five variants. Each α variant has a BOR with the parent β grain, i.e. the $\{0001\}_\alpha \| \{110\}_\beta$ planes shown in Fig. 17 by the overlapping poles in red in each basal plane of the α variants, and slip directions $<11\bar{2}0>_\alpha \| <111>_\beta$ by the green markers showing the angular difference of the $<1\bar{2}10>_\alpha$ direction of 10.5° off from $<\bar{1}11>_\beta$. Note that each of the α variants has different crystal orientation. The boundary conditions for each microstructure model are given in Fig. 16(c), (f) and (i).

Fig. 18 shows the strain rate sensitivity results obtained from the crystal plasticity modelling for a pure α phase (with basal slip only) single crystal, the colony structure shown in Fig. 16(a) the globular equiaxed microstructure in Fig. 16(d) and the basket weave structure given in Fig. 16(g) with the microstructural form labelled on the horizontal axis. The basket weave structure is also included for the case in which the five differing α variants are simplified to a single variant, referred as basketweave (no variant) in Fig. 18. Strain rate calculations were carried out for two loading regimes with tensile straining up to a strain of 2% in the X- and Y-directions respectively. For the single crystal, colony, and basket weave microstructures, strong anisotropy (with loading direction) is expected because of the small number of microstructural units whereas for the equiaxed globular structure, with many units, a much more isotropic response is anticipated. The results in Fig. 18 reflect these expectations.

The α single crystal (with basal slip only) and the colony structure exhibit strong anisotropy in vertical (Y-) and transverse (X-) direction loadings. The globular equiaxed microstructure, however, shows a lower strain rate sensitivity (for the boundary conditions given in Fig. 16), indicating again the importance of constraint imposed by grains and their boundaries on rate sensitivity. This is a consistent finding for polycrystals when compared to single crystals and single colonies. The globular equiaxed microstructure also shows isotropic strain rate sensitivity, reflecting the random texture assignment, and

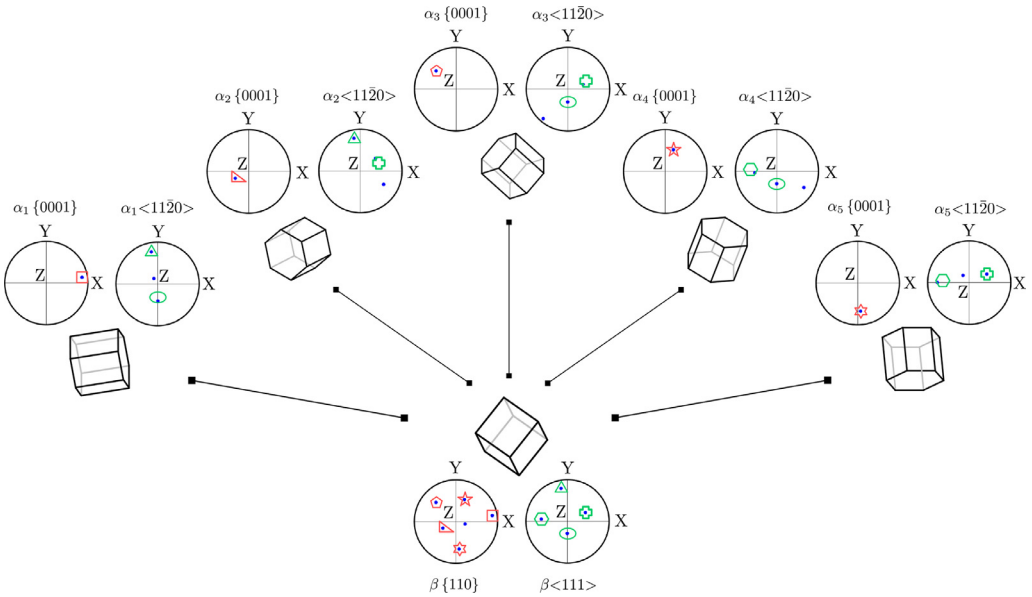

Fig. 17. Microscale kinematic confinement in basketweave structures: transformed β grain in the left of Fig. 16(h) and its five α variants with orientations shown. (For interpretation of the references to colour in the text, the reader is referred to the web version of this article.)

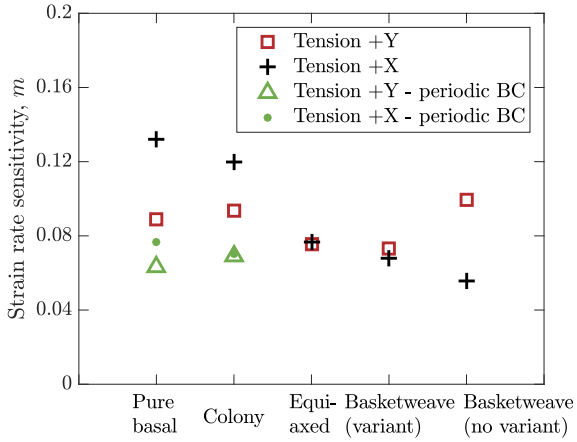

Fig. 18. Dependence of strain rate sensitivity on morphology: basketweave (no variant) behaves as colony structures.

the limited role played by β lath orientation, consistent with the earlier colony orientation studies. The anisotropy of intrinsic strain rate sensitivity can therefore be counteracted to some extent to become more isotropic through (random) texture control. The basket weave microstructure with α variants gives lower strain rate sensitivity in Fig. 18, due to its much more complex structure involving the BOR between the β and α phases and the variants of the latter shown in Fig. 17, giving rise to considerable constraint and more so than that for the globular, equiaxed colony structures. Recent studies on α-β micro-pillar tests showed that the BOR may become violated through lattice rotation during deformation (Zhang et al., 2016b), although quite large deformations are needed ($> \sim 10\%$) for this to become observable. To assess further the role of the α variants and the BOR in the basket weave microstructure, with respect to the globular equiaxed microstructure, the basket weave variants are simplified to retain only a single variant with the BOR. The effect of this is to make the basket weave structure much closer in response to the colony type behaviour and the strain rate sensitivity becomes anisotropic as shown in Fig. 18. The SRS for the Y-direction loading is significantly higher because of the preference for basal slip to be activated with this loading, compared to that in the X-direction which favours prism slip and gives a lower SRS. As shown in Fig. 18 by the green symbols for the pure α and colony structure, the polycrystalline confinement effect, realized through periodic boundary condition, tends to decrease the strain rate sensitivity. Interestingly, the resulting strain rate sensitivity is around 0.07, at the same level as the equiaxed and basket weave (with variants) levels. This strengthens the argument that for low ($< \sim 20\%$) volume fraction β alloys - the near-α alloys - the structural strain rate sensitivity is largely governed by the α phase, and the phenomenon of slip transmission between α and β phases as in the experiment by Zhang et al. (2016b) likely plays a secondary role, together with that of morphological effects. This conclusion, however, is confined

to near-α Ti-6242 where the β phase volume fraction is low and not representative of alloy Ti-6246 that generally has 40%−50% β phase. The impact of morphological effect due to basket weave microstructure is likely to be significant in reducing/inhibiting the rate dependence/creep performance in Ti-6246, since it has much greater likelihood to have multiple α variants in the transformed β grains as well as greater possibilities of homogenized behaviour.

The present study may be contextualised with reference to the creep behaviours which result from differing morphologies. It has been found that basketweave microstructures, containing multiple colonies of α and β laths within prior β grains, is more creep resistant than the bimodal microstructure in Ti-6242Si (Bania and Hall, 1985). In addition, this basket weave morphological pattern has also been reported to have stronger creep resistance than colony structures in Ti-6242. Suri et al. (1997) found that basket weave structures in Ti-6242 have much finer colony size than those in the globular equiaxed microstructures and the accumulated creep strain was expected to be smaller in basket weave structures. Miller et al. (1987) found creep strains to be smaller in basket weave structures compared to colony structures in Ti-6Al-2Nb-1Ta-0.8Mo alloy. They argued that larger colony sizes led to larger creep strains and that smaller colony size provided shorter distances to accommodate slip, and that basket weave structure exhibits limited slip compatibility.

4. Summary and conclusions

In this paper, we began from the recently measured intrinsic strain rate sensitivities of HCP α basal and prismatic and BCC β slip systems in alloy Ti-6242 in order to address structural strain rate sensitivities in colonies, bimodal and basket weave microstructures, including the effects of α variants.

Intrinsic HCP α Ti slip system strain rate sensitivities give rise to single crystal and $\alpha-\beta$ colony structure rate sensitivities which are highly directionally anisotropic. We introduce the term 'structural strain rate sensitivity' to describe the response characterised by the exponent m in $\sigma = k\dot{\varepsilon}^m$ and provide its relationship to intrinsic activation energy and volume for thermally activated dislocation-controlled slip, and crystallographic orientation. In colony structures, where the volume fraction of β phase remains below ~20% in alloy Ti-6242, the structural strain rate sensitivity is controlled by the α phase response; the effect of β lath orientation and volume fraction are found to be negligible. In addition, the apparent anisotropy of resolved shear stresses on the a_1, a_2 and a_3 basal slip systems for slip activation reported in the literature for $\alpha-\beta$ colony structures has been found to derive from local stress states within the colony which are not uniaxial. The more complex stress states which affect the resolved shear stresses originate from the asymmetry of the HCP α crystal axes with respect to the loading direction as opposed to the $\alpha-\beta$ interfaces.

The effect of constraint, provided either by polycrystal effects (surrounding grains, boundaries) or periodic boundary conditions (e.g. for simple single colony structures), leads to considerable reductions in strain rate sensitivity. Hence, the strain rate sensitivities extracted from micro-pillar tests are considerably higher than those for polycrystal response where constraint effects are significant. Neeraj et al. (2000) found the macroscopic strain rate sensitivity to be about 0.02 in both Ti-6Al (a single α phase Ti alloy) and Ti-6242 (near α-Ti). They obtained the strain rate sensitivity by fitting the Hollomon flow equation $\sigma = k\varepsilon^n\dot{\varepsilon}^m$ to the room temperature compressive creep tests on ~12 mm specimens. Their measured strain rate sensitivities remain considerably lower than those found in this study (~0.05) which were determined from knowledge of the intrinsic micro-pillar rate sensitivities. This indicates that there remain mechanistic aspects which have not been captured in the present crystal plasticity modelling particularly in linking intrinsic, unconstrained single crystal slip system rate sensitivities to constrained, polycrystal rate-sensitive behaviour. While introducing boundary constraint leads to significant reductions in predicted polycrystal rates sensitivities, it is apparent that there are additional constraints not yet represented in the present CP modelling. A hypothesis is that the remaining differences result from the absence of discrete dislocation and pile-up events in the context of explicit modelling grain boundary constraint which could influence local strain rate sensitivity. Further investigation to consider this effect is underway.

Polycrystal texture, $\alpha-\beta$ morphology and constraint in alloy Ti-6242 all affect the structural strain rate sensitivity; strong textures can lead to significant and measurable changes in strain rate sensitivities which have been observed in independent experiments. Colony, bimodal, and basket weave microstructures in Ti-6242 give differing strain rate sensitivities where, for the latter two, similar random textures are present. However, the intrinsic rate sensitivity of the HCP α phase dominates the polycrystal rate-sensitive behaviour. In the basket weave structure, however, the HCP α phase variants in conjunction with the BORs do show considerable effects on structural strain rate sensitivity, with a higher number of variants being present tending to reduce the strain rate sensitivity. A consequence is that higher numbers of variants occurring in the alloy (e.g. Ti-6246) may inhibit dwell fatigue debit.

An orientation dependent rate sensitivity has been reported in many different cubic and hexagonal crystalline materials so that the present micro-mechanical study may be generalized or extended to other heterogeneous alloys in the following aspects: (1) the role of intrinsic strain rate sensitivity in differing slip systems and different phases; (2) the proposed rate sensitive mechanisms applicable for low temperature ($T < 0.3Tm$) material creep in low and high stress states; (3) the role of microscale kinematic confinement due to surrounding grains or phases; (4) multiphase alloy rate sensitive behaviour.

Acknowledgements

The authors gratefully acknowledge the Engineering & Physical Science Research Council for funding through HexMat (EP/K034332). Further details of the HexMat grant can be found at http://www.imperial.ac.uk/hexmat. Zhen owes thankful

gratitude to Drs Joseph Sudha and Tea-Sung Jun for images of bimodal equiaxed and basket weave microstructures, respectively. FPED would like to acknowledge the Royal Academic of Engineering for additional funding for his research chair.

Data underpinning this work is available via Zenodo at https://zenodo.org/record/437779#.WNPRhG-LSUk and is openly available under a Creative Commons CC-BY licence.

Appendix A. Stress drop and time constant

Since the deformation is held constant during stress relaxation, the strain rate partitioning gives

$$\dot{\varepsilon} = \dot{\varepsilon}_e + \dot{\varepsilon}_p = 0 \tag{a.1}$$

The elastic strain rate is given by

$$\dot{\varepsilon}_e = \frac{1}{E}\frac{d\sigma}{dt} \tag{a.2}$$

Based on Eq. (5), Eq. (a.1) then gives

$$\frac{d\sigma}{dt} + \eta EM \sinh\left[\chi M(\sigma - \sigma_c)\right] = 0 \tag{a.3}$$

The stress-time relation during stress relaxation can then be obtained from Eq. (a.3) as

$$\sigma(t) = \sigma_c + \frac{1}{\chi M}\ln\left[\tanh\left((1+\frac{t}{c})\frac{\eta EM^2\chi c}{2}\right)\right] \tag{a.4}$$

where c is a constant determined by the initial conditions.

Taking the stress at the start of stress hold at $t = 0$, to be $\sigma(0)$, then the constant c is determined by

$$c = \frac{2}{\mathrm{EM}^2\eta\chi}\mathrm{arctanh}\{\exp[\chi \mathrm{M}(\sigma(0) - \sigma_c)]\} \tag{a.5}$$

The stress drop is given by

$$\Delta\sigma = \sigma(0) - \sigma(t) = \frac{1}{\chi M}\left\{\ln\left[\tanh\left(\frac{EM^2\eta\chi c}{2}\right)\right] - \ln\left[\tanh\left((1+\frac{t}{c})\frac{EM^2\eta\chi c}{2}\right)\right]\right\} \tag{a.6}$$

Appendix B

This appendix shows the crystal orientations used in Section 3. In particular, the three orientations in α-basal colony (in Table b.1) are obtained by matching the available Schmid factors in the α phase (i.e. in Tables b.2 and b.3), and at the

Table b.1
Euler angles used in colony structures in Section 3.1.

Unit cell α-β colony		α (°)	β (°)
Basal*	a_1	[24 51−95]	[−135 175 110]
	a_2	[−142 119 −122]	[59 101 114]
	a_3	[−38 120 −177]	[−169 73 151]
Prism*	a_1	[−90 20 165]	[151 127−117]
	a_2	[−135 0 0]	[−43 134 −93]
	a_3	[−165 0 0]	[−73 134−93]

* Crytal orientaitons of a_2-basal and a_2-prism are used in Section 3.2.

Table b.2
Comparison of reproduced Schmid factor (with Euler angles in Table b.1 and loading in global Y axis in Fig. 6) with those in Savage et al. (2004) on α phase and basal systems active only.

Plane	Slip system	Schmid factor					
		a_1 basal	a_2 basal	a_3 basal	a_1 basal	a_2 basal	a_3 basal
		Savage et al. (2004)					
		$(2\bar{1}\bar{1}3)$	$(\bar{1}2\bar{1}3)$	$(\bar{1}\bar{1}23)$	$(2\bar{1}\bar{1}3)$	$(\bar{1}2\bar{1}3)$	$(\bar{1}\bar{1}23)$
Basal	$[\bar{2}110](0001)$	0.5	0.25	0.25	0.50	0.25	0.25
	$[\bar{1}2\bar{1}0](0001)$	0.25	0.5	0.25	0.25	0.50	0.25
	$[\bar{1}\bar{1}20](0001)$	0.25	0.25	0.5	0.25	0.25	0.50
Prism	$[\bar{2}110](0001)$	0.00	0.23	0.23	0.00	0.23	0.23
	$[\bar{1}2\bar{1}0](0001)$	0.23	0.00	0.23	0.22	0.00	0.23
	$[\bar{1}\bar{1}20](0001)$	0.23	0.23	0.00	0.22	0.23	0.00
Pyramidal	$[\bar{2}110](0\bar{1}11)$	0.24	0.32	0.32	0.24	0.32	0.32
	$[\bar{2}110](0\bar{1}11)$	0.24	0.08	0.08	0.24	0.08	0.08
	$[\bar{1}2\bar{1}0](10\bar{1}1)$	0.32	0.24	0.32	0.31	0.24	0.08
	$[\bar{1}2\bar{1}0](\bar{1}011)$	0.08	0.24	0.08	0.07	0.24	0.32
	$[\bar{1}\bar{1}20](1\bar{1}01)$	0.32	0.32	0.24	0.31	0.32	0.24
	$[\bar{1}\bar{1}20](1\bar{1}0\bar{1})$	0.08	0.08	0.24	0.07	0.08	0.24

Table b.3
Comparison of reproduced Schmid factor (with Euler angles in Table b.1 and loading in global Y axis in Fig. 6) with those in Savage et al. (2004) on β phase and basal systems active only.

Plane	Slip system	Schmid factor					
		a_1 basal Savage et al. (2004)	a_2 basal Savage et al. (2004)	a_3 basal Savage et al. (2004)	a_1 basal	a_2 basal	a_3 basal
		$(2\bar{1}\bar{1}3)$	$(\bar{1}2\bar{1}3)$	$(\bar{1}\bar{1}23)$	$(2\bar{1}\bar{1}3)$	$(\bar{1}2\bar{1}3)$	$(\bar{1}\bar{1}23)$
b1	$[11\bar{1}](101)$	0.5	0.25	0.25	0.50	0.26	0.23
	$[11\bar{1}](011)$	0.25	0.07	0.07	0.25	0.35	0.30
	$[11\bar{1}](\bar{1}10)$	0.25	0.32	0.32	0.25	0.09	0.07
	$[11\bar{1}](112)$	0.43	0.10	0.10	0.43	0.35	0.30
	$[11\bar{1}](\bar{1}21)$	0	0.23	0.23	0.00	0.25	0.22
	$[11\bar{1}](\bar{2}1\bar{1})$	0.43	0.33	0.33	0.43	0.10	0.09
b2	$[\bar{1}11](101)$	0.17	0.50	0.32	0.17	0.31	0.49
	$[\bar{1}11](110)$	0.23	0.33	0.05	0.23	0.39	0.19
	$[\bar{1}11](01\bar{1})$	0.06	0.16	0.06	0.06	0.08	0.31
	$[\bar{1}11](211)$	0.23	0.47	0.41	0.23	0.40	0.39
	$[\bar{1}11](\bar{1}\bar{2}1)$	0.17	0.10	0.26	0.17	0.27	0.07
	$[\bar{1}11](\bar{1}1\bar{2})$	0.06	0.37	0.15	0.06	0.13	0.46
b3	$[111](\bar{1}10)$	0.28	0.32	0.13	0.28	0.21	0.17
	$[111](01\bar{1})$	0.20	0.08	0.12	0.20	0.17	0.32
	$[111](\bar{1}01)$	0.48	0.25	0.01	0.48	0.04	0.49
	$[11\bar{1}](\bar{2}11)$	0.43	0.32	0.08	0.43	0.15	0.38
	$[11\bar{1}](\bar{1}2\bar{1})$	0.04	0.25	0.14	0.04	0.22	0.09
	$[11\bar{1}](\bar{1}\bar{1}2)$	0.40	0.10	0.06	0.39	0.08	0.47
b4	$[1\bar{1}1](011)$	0.11	0.15	0.20	0.11	0.10	0.32
	$[1\bar{1}1](110)$	0.30	0.34	0.13	0.30	0.09	0.09
	$[1\bar{1}1](\bar{1}01)$	0.19	0.48	0.07	0.19	0.00	0.23
	$[1\bar{1}1](\bar{1}12)$	0.03	0.37	0.15	0.05	0.06	0.32
	$[1\bar{1}1](121)$	0.24	0.11	0.19	0.23	0.11	0.24
	$[1\bar{1}1](\bar{2}\bar{1}1)$	0.28	0.48	0.04	0.28	0.05	0.08

same time BOR relations are maintained to identify the β phase orientation. The crystal orientations of a_2 prism colony are determined by ensuring the global Schmid factor is 0.5 in α phase. Then the β phase orientation is obtained by imposing BOR relations.

References

Abdolvand, H., Daymond, M.R., Mareau, C., 2011. Incorporation of twinning into a crystal plasticity finite element model: evolution of lattice strains and texture in Zircaloy-2. Int. J. Plast. 27, 1721–1738.

Acharya, A., Beaudoin, A., Miller, R., 2008. New perspectives in plasticity theory: dislocation nucleation, waves, and partial continuity of plastic strain rate. Math. Mech. Solids 13, 292–315.

Adenstedt, H., 1949. Creep of titanium at room temperature. Met. Prog. 56, 658–660.

Amouzou, K., Richeton, T., Roth, A., Lebyodkin, M., Lebedkina, T., 2016. Micromechanical modeling of hardening mechanisms in commercially pure α-titanium in tensile condition. Int. J. Plast. 80, 222–240.

Ankem, S., Margolin, H., 1986. A rationalization of stress-strain behavior of two-ductile phase alloys. Metall. Trans. 17, 2209–2226.

Asaro, R.J., Suresh, S., 2005. Mechanistic models for the activation volume and rate sensitivity in metals with nanocrystalline grains and nano-scale twins. Acta Mater. 53, 3369–3382.

Bache, M.R., 2003. A review of dwell sensitive fatigue in titanium alloys: the role of microstructure, texture and operating conditions. Int. J. Fatigue 25, 1079–1087.

Bania, P., Hall, J., 1985. Creep studies of Ti-6242-Si alloy. Titanium 2371–2378.

Bonneville, J., Escaig, B., 1979. Cross-slipping process and the stress-orientation dependence in pure copper. Acta Metall. 27, 1477–1486.

Caillard, D., Martin, J.-L., 2003. Thermally Activated Mechanisms in Crystal Plasticity. Elsevier.

Canova, G., Fressengeas, C., Molinari, A., Kocks, U., 1988. Effect of rate sensitivity on slip system activity and lattice rotation. Acta Metall. 36, 1961–1970.

Cho, W., Jones, J., Allison, J., Donlon, W., 1988. Creep behavior of Ti-6242: the effect of microstructure and silicon content. In: Sixth World Conference on Titanium. I, pp. 187–192.

Conrad, H., 1981. Effect of interstitial solutes on the strength and ductility of titanium. Prog. Mater. Sci. 26, 123–404.

Conrad, H., Hays, L., Schoeck, G., Wiedersich, H., 1961. On the rate-controlling mechanism for plastic flow of Mg crystals at low temperatures. Acta Metall. 9, 367–378.

Conrad, H., Wiedersich, H., 1960. Activation energy for deformation of metals at low temperatures. Acta Metall. 8, 128–130.

Dieter, G.E., Bacon, D.J., 1986. Mechanical Metallurgy. McGraw-Hill, New York.

Donachie, M.J., 2000. Titanium: A Technical Guide. ASM International, Materials Park, OH.

Dunne, F.P.E., Rugg, D., Walker, A., 2007. Lengthscale-dependent, elastically anisotropic, physically-based hcp crystal plasticity: application to cold-dwell fatigue in Ti alloys. Int. J. Plasticity 23, 1061–1083.

Evans, A.G., Rawlings, R.D., 1969. The thermally activated deformation of crystalline materials. Physica Status Solidi 34, 9–31.

Evans, W., 1987. Creep-fatigue interactions in Ti-6 Al-4 V at ambient temperatures. Creep Fract. Eng. Mater. Struct. 603–613.

Evans, W., 1998. Optimising mechanical properties in alpha+ beta titanium alloys. Mater. Sci. Eng. 243, 89–96.

Eyring, H., 1936. Viscosity, plasticity, and diffusion as examples of absolute reaction rates. J. Chem. Phys. 4, 283–291.

Feltham, P., 1960. Stress relaxation in copper and alpha-brasses at low temperatures. J. Inst. Metall. 89, 210–214.

Feltham, P., 1961. Creep and stress relaxation in alpha-brass at low temperatures. Phil. Mag. 6, 259–270.

Feltham, P., 1963. Stress relaxation in magnesium at low temperatures. Physica Status Solidi 3, 1340–1346.

Gibbs, G.B., 1969. Thermodynamic analysis of dislocation glide controlled by dispersed local obstacles. Mater. Sci. Eng. 4, 313–328.
Gong, J., Wilkinson, A.J., 2009. Anisotropy in the plastic flow properties of single-crystal α titanium determined from micro-cantilever beams. Acta Mater. 57, 5693–5705.
Gu, H., Guo, H., Chang, S., Campbell, L., 1994. Orientation dependence of cyclic deformation in high purity titanium single crystals. Mater. Sci. Eng. 188, 23–36.
Guiu, F., Pratt, P., 1964. Stress relaxation and the plastic deformation of solids. Physica Status Solidi 6, 111–120.
Guiu, F., Pratt, P., 1966. The effect of orientation on the yielding and flow of molybdenum single crystals. Phys. Status Solidi 15, 539–552.
Hirth, J., Nix, W., 1969. An analysis of the thermodynamics of dislocation glide. Physica Status Solidi (b) 35, 177–188.
Inui, H., Matsumuro, M., Wu, D.H., Yamaguchi, M., 1997. Temperature dependence of yield stress, deformation mode and deformation structure in single crystals of TiAl (Ti-56 at% Al). Philos. Mag. A 75, 395–423.
Izadi, E., Rajagopalan, J., 2016. Texture dependent strain rate sensitivity of ultrafine-grained aluminum films. Scr. Mater. 114, 65–69.
Jun, T.-S., Armstrong, D.E., Britton, T.B., 2016a. A nanoindentation investigation of local strain rate sensitivity in dual-phase Ti alloys. J. Alloys Compd. 672, 282–291.
Jun, T.-S., Zhang, Z., Sernicola, G., Dunne, F.P., Britton, T.B., 2016b. Local strain rate sensitivity of single α phase within a dual-phase Ti alloy. Acta Mater. 107, 298–309.
Kocks, U.F., Argon, A.S., Ashby, M.F., 1975. Thermodynamics and kinetics of slip. Prog. Mater. Sci. 19, 1–281.
Korla, R., Chokshi, A.H., 2010. Strain-rate sensitivity and microstructural evolution in a Mg–Al–Zn alloy. Scr. Mater. 63, 913–916.
Kumar, R.S., Wang, A.J., McDowell, D.L., 2006. Effects of microstructure variability on intrinsic fatigue resistance of nickel-base superalloys–a computational micromechanics approach. Int. J. Fract. 137, 173–210.
Leverant, G., Kear, B., Oblak, J., 1973. Creep of precipitation-hardened nickel-base alloy single crystals at high temperatures. Metall. Trans. 4, 355–362.
Lutjering, G., 1998. Influence of processing on microstructure and mechanical properties of (alpha+beta) titanium alloys. Mater. Sci. Eng. A 243, 32–45.
Lütjering, G., Williams, J.C., 2007. Titanium. Springer, Berlin Heidelberg.
May, K., 2010. Small Scale Tensile Testing of Titanium Alloys Mater thesis. Ohio State University, Columbus, Ohio.
Mayeur, J.R., McDowell, D.L., 2007. A three-dimensional crystal plasticity model for duplex Ti–6Al–4V. Int. J. Plast. 23, 1457–1485.
Meyers, M.A., Mishra, A., Benson, D.J., 2006. Mechanical properties of nanocrystalline materials. Prog. Mater. Sci. 51, 427–556.
Miller, W., Chen, R., Starke, E., 1987. Microstructure, creep, and tensile deformation in Ti-6Al-2Nb-1Ta-0.8 Mo. Metall. Trans. A 18, 1451–1468.
Neeraj, T., Hou, D.H., Daehn, G.S., Mills, M.J., 2000. Phenonomenological and microstructural analysis of room temperature creep in titanium alloys. Acta Mater. 48, 1225–1238.
Pettermann, H.E., Suresh, S., 2000. A comprehensive unit cell model: a study of coupled effects in piezoelectric 1–3 composites. Int. J. Solids Struct. 37, 5447–5464.
Qiu, J., Ma, Y., Lei, J., Liu, Y., Huang, A., Rugg, D., Yang, R., 2014. A comparative study on dwell fatigue of Ti-6Al-2Sn-4Zr-xMo (x= 2 to 6) alloys on a microstructure-normalized basis. Metall. Mater. Trans. A 45, 6075–6087.
Rae, C., Reed, R., 2007. Primary creep in single crystal superalloys: origins, mechanisms and effects. Acta Mater. 55, 1067–1081.
Rose, R.M., 1962. Yielding and plastic flow in single crystals of tungsten. Trans. Met. Soc. AIME 224, 981–989.
Savage, M., Tatalovich, J., Zupan, M., Hemker, K., Mills, M., 2001. Deformation mechanisms and microtensile behavior of single colony Ti–6242Si. Mater. Sci. Eng. 319, 398–403.
Savage, M.F., Tatalovich, J., Mills, M.J., 2004. Anisotropy in the room-temperature deformation of alpha-beta colonies in titanium alloys: role of the alpha–beta interface. Philos. Mag. 84, 1127–1154.
Seeger, A., 1954. The temperature dependence of the critical shear stress and of work-hardening of metal crystals. London Edinb. Dubl. Philos. Mag. J. Sci. 45, 771–773.
Sinha, V., Mills, M., Williams, J., 2006. Crystallography of fracture facets in a near-alpha titanium alloy. Metall. Mater. Trans. A 37, 2015–2026.
Spitzig, W.A., Keh, A.S., 1970. Orientation dependence of the strain-rate sensitivity and thermally activated flow in iron single crystals. Acta Metall. 18, 1021–1033.
Suri, S., Neeraj, T., Daehn, G.S., Hou, D.H., Scott, J.M., Hayes, R.W., Mills, M.J., 1997. Mechanisms of primary creep in alpha/beta titanium alloys at lower temperatures. Mater. Sci. Eng. A 234, 996–999.
Suri, S., Viswanathan, G.B., Neeraj, T., Hou, D.H., Mills, M.J., 1999. Room temperature deformation and mechanisms of slip transmission in oriented single–colony crystals of an alpha/beta titanium alloy. Acta Mater. 47, 1019–1034.
Taylor, G., 1992. Thermally-activated deformation of BCC metals and alloys. Prog. Mater Sci. 36, 29–61.
Thornton, P., Hirsch, P., 1958. The effect of stacking fault energy on low temperature creep in pure metals. Philos. Mag. 3, 738–761.
Umakoshi, Y., Nakano, T., Takenaka, T., Sumimoto, K., Yamane, T., 1993. Orientation and temperature dependence of yield stress and slip geometry of Ti3Al and Ti3Al-V single crystals. Acta Metall. Mater. 41, 1149–1154.
Van der Sluis, O., Schreurs, P., Brekelmans, W., Meijer, H., 2000. Overall behaviour of heterogeneous elastoviscoplastic materials: effect of microstructural modelling. Mech. Mater. 32, 449–462.
Viswanathan, G., Karthikeyan, S., Hayes, R., Mills, M., 2002. Creep behaviour of Ti-6Al-2Sn-4Zr-2Mo: II. Mechanisms of deformation. Acta Mater. 50, 4965–4980.
Wang, Y., Hamza, A., Ma, E., 2006. Temperature-dependent strain rate sensitivity and activation volume of nanocrystalline Ni. Acta Mater. 54, 2715–2726.
Weertman, J., 1983. Creep deformation of ice. Annu. Rev. Earth Planet. Sci. 11, 215.
Wei, Q., 2007. Strain rate effects in the ultrafine grain and nanocrystalline regimes—influence on some constitutive responses. J. Mater. Sci. 42, 1709–1727.
Weiss, I., Semiatin, S., 1998. Thermomechanical processing of beta titanium alloys - an overview. Mater. Sci. Eng. 243, 46–65.
Weiss, I., Semiatin, S., 1999. Thermomechanical processing of alpha titanium alloys - an overview. Mater. Sci. Eng. 263, 243–256.
Welsch, G., Boyer, R., Collings, E., 1993. Materials Properties Handbook: Titanium Alloys. ASM international.
Williams, J., Baggerly, R., Paton, N., 2002. Deformation behavior of HCP Ti-Al alloy single crystals. Metall. Mater. Trans. A 33, 837–850.
Williams, J.C., Mills, M.J., Rokhlin, S., 2006. The Evaluation of Cold Dwell Fatigue in Ti-6242 FAA Report Summary.
Zhang, Z., Cuddihy, M.A., Dunne, F.P.E., 2015. On rate-dependent polycrystal deformation: the temperature sensitivity of cold dwell fatigue. Proc. R. Soc. A 471, 20150214.
Zhang, Z., Eakins, D.E., Dunne, F.P.E., 2016a. On the formation of adiabatic shear bands in textured HCP polycrystals. Int. J. Plast. 79, 196–216.
Zhang, Z., Jun, T.-S., Britton, T.B., Dunne, F.P.E., 2016b. Determination of Ti-6242 alpha and beta slip properties using micro-pillar test and computational crystal plasticity. J. Mech. Phys. Solids 95, 393–410.
Zhang, Z., Jun, T.-S., Britton, T.B., Dunne, F.P.E., 2016c. Intrinsic anisotropy of strain rate sensitivity in single crystal alpha titanium. Acta Mater. 118, 317–330.
Zheng, Z., Balint, D.S., Dunne, F.P.E., 2016. Dwell fatigue in two Ti alloys: an integrated crystal plasticity and discrete dislocation study. J. Mech. Phys. Solids In press.
Zhu, T., Li, J., Samanta, A., Kim, H.G., Suresh, S., 2007. Interfacial plasticity governs strain rate sensitivity and ductility in nanostructured metals. Proc. Natl. Acad. Sci. 104, 3031–3036.